Bioactive and chemically defined hydrogels with tunable stiffness guide cerebral organoid formation and modulate multi-omics plasticity in cerebral organoids

Melis Isik[1], Babatunde O. Okesola[2], Cemil Can Eylem[3], Engin Kocak[4], Emirhan Nemutlu[3,5], Matteo D'Este[6], Alvaro Mata[7,8], and Burak Derkus[1*]

1. Stem Cell Research Lab, Department of Chemistry, Faculty of Science, Ankara University, Ankara 06560, Turkey
2. School of Life Sciences, Faculty of Medicine and Health Sciences, University of Nottingham, Nottingham NG7 2UH, UK
3. Analytical Chemistry Division, Faculty of Pharmacy, Hacettepe University, 06230 Ankara, Turkey
4. Division of Analytical Chemistry, Faculty of Gulhane Pharmacy, Health Science University, Ankara 06018, Turkey
5. Bioanalytic and Omics Laboratory, Faculty of Pharmacy, Hacettepe University, Ankara, Turkey
6. AO Research Institute Davos, Clavadelerstrasse 8, Davos Platz 7270, Switzerland
7. School of Pharmacy University of Nottingham, University Park, NG7 2RD, Nottingham, UK
8. Department of Chemical and Environmental Engineering, University of Nottingham, University Park, NG7 2RD, Nottingham, UK

*Corresponding Author: bderkus@ankara.edu.tr

ABSTRACT

Organoids are an emerging technology with great potential in human disease modelling, drug development, diagnosis, tissue engineering, and regenerative medicine. Organoids as 3D-tissue culture systems have gained special attention in the past decades due to their ability to faithfully recapitulate the complexity of organ-specific tissues. Despite considerable successes in culturing physiologically relevant organoids, their real-life applications are currently limited by challenges such as scarcity of an appropriate biomimetic matrix. Peptide amphiphiles (PAs) due to their well-defined chemistry, tunable bioactivity, and extracellular matrix (ECM)-like nanofibrous architecture represent an attractive material scaffold for organoids development. Using cerebral organoids (COs) as exemplar, we demonstrate the possibility to create bio-instructive hydrogels with tunable stiffness ranging from 0.69 kPa to 2.24 kPa to culture and induce COs growth. We used orthogonal chemistry involving oxidative coupling and

supramolecular interactions to create two-component hydrogels integrating the bio-instructive activity and ECM-like nanofibrous architecture of a laminin-mimetic PAs (IKVAV-PA) and tunable crosslinking density of hyaluronic acid functionalized with tyramine (HA-Try). Multi-omics technology including transcriptomics, proteomics, and metabolomics reveals the induction and growth of COs in soft HA-Tyr hydrogels containing PA-IKVAV such that the COs display morphology and biomolecular signatures similar to those grown in Matrigel scaffolds. Our materials hold great promise as a safe synthetic ECM for COs induction and growth. Our approach represents a well-defined alternative to animal-derived matrices for the culture of COs and might expand the applicability of organoids in basic and clinical research.

Keywords: Peptide amphiphiles, hyaluronic acid, hydrogel, mechanotransduction, cerebral organoid, omics

1. Introduction

Recent advances in 3-dimensional (3D) cell culture technologies allow pluripotent and primary cells to exhibit their remarkable self-organizing potential and capacity to generate organoids with capability to recapitulate key morphological and functional properties of organs. Organoid is an emerging technology first created in 2008 to model the human cortical organ [1]. Since then, various types of organoids aiming to model different organs such as lung [2], stomach [3], kidney [4], liver [5], and small intestine [6] or specialized parts of an organ such as adenohypophysis [7], hippocampus [8], and cerebellar [9] organoids have been reported. A critical step in the growth of these organoid systems requires the growth of cells in Matrigel, a solubilized basement membrane extracted from mouse sarcoma and consists of an undefined mixture of ECM components. For instance, a recent study has shown that the brain and some other organoids can only be effectively produced within Matrigel scaffolds [10]. However, its murine origin, batch-to-batch variation, immunogenic and tumorigenic potential, and high cost [11] represent major challenges for the clinical use of Matrigel. Given these limitations, there is an urgent need for chemically-defined replacement matrices that can grow organoids in a more reproducible, clinically relevant, and feasible manner.

A variety of materials have been explored as substitutes for Matrigel to culture organoids [12]. Synthetic hydrogel with tunable mechanical properties created with polyethylene glycol (PEG), have been used for intestinal organoid culture [13]. However, the inert nature of PEG requires chemical modification with bioactive molecules such as RGD (Arg-Gly-Asp) peptides [13].

Similarly, 4-arm PEG-based hydrogels modified with maleimide (PEG-4MAL) enabled robust and reproducible *in vitro* growth and expansion of human intestinal organoids [14]. In another example, poly(lactide-co-glycolide) (PLGA) microfibres were used to direct the orientation of cerebral organoids (COs) into elongated embryoid bodies (EBs), enhance neuroepithelium, and improve cortical development [15]. Hydrogels composed of natural polymers including collagen, fibrin, hyaluronic acid, fibronectin, alginate, and their combinations have been used to culture stem cells and organoids providing them with biochemical, biophysical, and mechanical cues. For example, the possibility to grow COs in decellularized ECMs [16] and modified hyaluronic acid (HA) hydrogels [16,17] have been reported previously. Importantly, HA hydrogels have been shown to promote caudalizing effect on neural spheroids [17] and support the growth and expansion of 3 mm wide COs [18]. Notwithstanding, most of the synthetic and natural matrices used till date for organoids growth lack the appropriate physico-mechanical features of the native tissue microenvironment. Peptide amphiphiles (PAs) are an attractive synthetic ECM for cell culture and signalling due to their modularity intrinsic propensity to assemble into 3D hydrogels with ECM-mimetic sample spanning network of nanofibers [19]. These molecules consist of three main regions including a hydrophobic tail that drives self-assembly, a β-sheet forming amino acid sequence that stabilizes the assembled nanofibres, and a functional group that is designed to be displayed on the surface of the resulting nanofibres. This functional group can be short epitopes that elicit specific bioactivity such as stimulation of osteoblastic [20] and neurogenic [21,22] differentiations *in vitro* or promoting the regeneration of bone [23] and nerve [24] tissues *in vivo*. PAs can also be co-assembled with ECM components to create 3D matrices with tuneable composition. For example, we have recently co-assembled PAs, with ECM-derived molecules to create hydrogels with tunable mechanics and bioactivity to control spheroids formation by various kinds of cancer cells [25, 26]. Nonetheless, to the best of our knowledge, the use of PA-based systems to grow, induce, and expand organoids has not been reported.

Beyond the molecular design of a suitable building blocks to create synthetic ECM for cell and organoids culture, the ECM parameters including mechanical property and nanoscale morphology play crucial roles in the histogenesis and overall behavior of cells and organoids. The effects of matrix stiffness on cell differentiation, adhesion, migration, and apoptosis have been extensively studied in both 2D and 3D cultures. For instance, tunable hydrogel stiffness has been used to control the differentiation of mesenchymal stem cells (MSCs) into tissue-specific lineages [27]. Similarly, matrix stiffness has been used to stimulate human pluripotent

stem cells (hPSCs) differentiation into postmitotic neurons when cultured in a compliant matrix [28]. By tuning the stiffness of collagen-conjugated polyacrylamide hydrogel, Shkumatov et al reported the possibility to control cardiac organoid growth [29]. Similarly, Gjorevski et al [30] showed that high stiffness is required to enhance intestinal stem cell colony formation and organoid expansion. In contrast, Sorrentino et al showed that, an aberrant matrix stiffness can compromise the proliferative capacity of liver organoids [31].

The filamentous architecture of the native ECM can have a significant impact on cell mechanotransduction, growth factor signalling, long-distance cell-to-cell communication, and migrations [32-34]. The possibility to investigate the synergistic effects of bio-instructive epitope, nanofibrous architecture and matrix stiffness on COs induction and growth will represent a new frontier in organoid technology.

Here, we report on a co-assembling material platform to enable a Matrigel-free culture of COs in a chemically and mechanically defined microenvironments. Our materials design strategy integrates PAs bearing a laminin-derived epitopes (IKVAV) with tunable crosslinking density of HA functionalized with tyramine (HA-Tyr) to create hydrogels with ECM-mimetic bio-instructive activity, nanofibrous architecture, and tunable matrix stiffness. We have previously demonstrated the possibility to guide and promote the differentiation and growth of neurons using laminin motif IKVAV [22]. We anticipate that by tuning the crosslinking density of HA-Tyr using various concentrations of HA-Tyr, we can create hydrogels with tunable stiffness. Incorporation of a cationic IKVAV-PA into the anionic HA-Tyr hydrogels can enable the creation of synthetic ECM with an appropriate stiffness and bio-instructive cues for COs induction and growth. We anticipate that the matrix stiffness, bio-instructive activity and ECM-mimetic nanofibers will modulate the neural differentiation capacity of EBs. We reasoned that HRP/H_2O_2 mediated oxidative coupling of the phenolic group of HA-Tyr will enable the creation of hydrogels with tunable stiffness as we have previously demonstrated [35]. We hypothesized that by using the appropriate matrix stiffness and bio-instructive cues, we can modulate the compositions of COs at the gene, protein, and metabolite levels, leading to the identification of optimal conditions for the growth and expansion of COs. To establish this hypothesis, we cultured COs within HA-Tyr/IKVAV-PA hydrogels and carried out high-throughput multi-omics analyses including transcriptomics, proteomics, and metabolomics to reveal the underlying molecular mechanisms of matrix stiffness-induced and bio-instructive modulation of biomolecular structures in the developed COs. Although, transcriptomics and proteomics have been used to characterize endometrial and gastrointestinal organoids grown in

hydrogels [36, 37], the possibility to use transcriptomics, proteomics, and metabolomics to characterise COs grown in a material matrix will represent a new paradigm. We believe the high-throughput data generated through these techniques will contribute to the current state-of-the-art and also help researchers benchmark future alternative matrices for organoids culture.

2. Materials and Methods

2.1. Synthesis of PAs

We synthesised **IKVAV-PA** and **VKIVA-PA** using a standard 9-fluorenylmethoxycarbonyl (Fmoc)-based solid phase synthesis protocol on an automated peptide synthesizer (Liberty Blue, CEM, USA) followed by an alkylation reaction with palmitic acid at the *N*-terminal as previously demonstrated [19,20,22,23]. A Waters 2545 Binary Gradient high-performance liquid chromatography (HPLC) system with a preparative reverse-phase C18 column (X-Bridge prep OBD, 5 μm, 30×150 mm column, Waters, UK) was used for purification of the crude peptides using a water/acetonitrile (0.1% TFA) gradient. The molecular weight of PAs was confirmed by electrospray ionization mass spectrometry (ESI-MS) using a single quadrupole mass detector (SQ Detector 2, Waters, UK). Detailed explanation of PAs synthesis and purification are provided in the supplementary information. PAs were characterized on a zetasizer to determine the net charge, circular dichroism (CD) spectroscopy to confirm the β-sheet conformation, and transmission electron microscopy (TEM) to visualize nanoscale morphology of PAs (details procedures are presented in SI).

2.2. Preparation and characterization of HA-Tyr/PA hydrogels

We prepared hydrogels by injecting an aqueous solution of PAs (**IKVAV-PA** or **VKIVA-PA,** 2% wt.) into an aqueous solution of **HA-Tyr** (1 and 3% wt. containing 2U/ml HRP), and incubate for 10 min to allow initial supramolecular co-assembly followed by an oxidative coupling in the presence of H_2O_2 (2 mM). The control HA-Tyr hydrogels were prepared following the same method without incorporating of PAs. It is noteworthy that injection and mixing of H_2O_2 should be performed rapidly since gelation occurs very fast (<1 min).

HA-Tyr and HA-Tyr/PA hydrogels were characterized with dynamic oscillatory rheology on a Rheometer (TA Instruments, USA). An oscillatory frequency sweep was performed in the range of 0.1–100 Hz under the constant strain of 0.15% to assess the visco-elastic behavior of the gels. The microstructures of gels were investigated under scanning electron microscope (SEM,

FEI 430 Nova NanoSEM, USA). The samples after freeze-drying were sputter-coated with gold (Quorom SC7640 High Resolution Sputter Coater, Lewes, UK) and the images were acquired at 10-15 kV.

2.3. Cytocompatibility

We expanded human neural stem cells (hNSCs, Cell Applications, USA) on laminin-coated flasks in neural expansion medium (Cell Applications, USA, lot no: 80705) and incubated at 37 °C and 5% CO_2 conditions. The viability and proliferation of cells growing in HA-Tyr (1 and 3% wt.) and HA-Tyr/IKVAV-PA hydrogels with varying PA concentrations (0.1, 1, 2% wt.) were assessed using Calcein-AM and Ethidium Homodimer-1 (EthD-1) (Thermo Scientific, USA) staining as well as MTS assay (Biological Industries, USA) at various time points (detailed information is provided in SI). All experiments were performed with three replicates.

2.4. Inducing organoid growth by the conventional and proposed methods

Two different human induced pluripotent stem cell lines (hiPSCs, kindly donated by Dr. Yalin Yildirim, Department of Cardiovascular Surgery, University Heart & Vascular Center Hamburg, Germany) were expanded on Vitronectin (Thermo Scientific, USA)-coated 6-well plates in Essential 8^{TM} Medium (Thermo Scientific, USA). Rock inhibitor (10 μm, Y-27632, STEMCELL Technologies, Canada) was added to the medium in the first 24h of culture. Once confluence is reached, we washed the cells with DPBS (Thermo Scientific, USA) and detached with Accutase (Thermo Scientific, USA) to further expand the cells or to induce COs formation.

COs were obtained from hiPSCs following a well-established protocol [10] using a commercial kit (STEMdiff Cerebral Organoid Kit, STEMCELL Technologies, Canada). Briefly, hiPSCs (9.000 cell/well) were seeded on an ultra-low attachment plate (ULAP) in the EB formation medium, the medium was changed to neural induction medium when the EB size reached up to 500-600 μm. After 2 days of induction, the neuroepithelial tissues were embedded in Matrigel and the culture was maintained in neural expansion medium for 4 days. Lastly, the medium was switched to maturation medium for another 4 days. This protocol involves the use of a medium, which includes neural induction components (DMEM/F12, Neurobasal Medium, N2, insulin, MEM-NEAA, and Glutamax) [10], leading to the formation of principally forebrain identity compared to other identities.

Concurrently, we also tested the capacity of HA-Tyr and HA-Tyr/PA hydrogels to induce EBs towards neuroepithelial tissue and COs following a slightly modified protocol. In this case, we embedded EBs into the hydrogels before neuroepithelial induction to harness bioactivities of PAs. First, we suspended EBs (400-600 μm) in 96-well ULAPs containing HA-Tyr(1%), HA-Tyr(1%)/IKVAV-PA, HA-Tyr(3%)/IKVAV-PA, or HA-Tyr/VKIVA-PA pre-gelation solution, then H_2O_2 (2 mM) was added to trigger HRP-mediated oxidative coupling of HA-Tyr. It is also noteworthy that cross-linking of HA-Tyr was completed within 1 min, a fast cross-linking process that represents an advantage over the 30-60 min required for Matrigel formation. After inducing EBs with neural induction medium for 4 days, the media was changed to expansion medium for another 4 days. Lastly, emerged organoids were cultured in maturation medium for more than 4 days similar to the conventional protocol. COs for the downstream analyses were taken out by digesting the HA-Tyr or HA-Tyr/PA gels with hyaluronidase (Sigma, USA).

2.5. Gene expression analysis

The effect of matrix bioactivity on organoid formation was investigated by gene expression analyses. To this aim, the expressions of Nestin, PAX6, TUJ1, MAP2, FOXG1, and SATB2 were assessed in COs in comparison to EBs, which were grown in HA-Tyr(1%), HA-Tyr(1%)/IKVAV-PA, HA-Tyr(1%)/VKIVA-PA, and Matrigel. Analyses were performed with three technical and three biological replicates. 30 organoids were used for each samples for RNA isolation, which corresponds to 90 organoids per group when the three replicates per group is considered. It should also be noted that 10 organoids were grown in each hydrogel, and three hydrogels were combined to make 30 organoids per sample. This protocol was followed to obtained a sufficient amount of RNA for the gene expression analyses. Further explanations describing the reverse transcriptase-quantitative polymerase chain reaction (RT-qPCR) protocol as well as the list of the sequences of primers is available in the SI.

2.6. Histology and immunofluorescent staining of COs

COs were fixed in 4% paraformaldehyde for 20 min at 4°C followed by washing in PBS three times. COs were then treated in 30% (wt.) sucrose overnight and embedded in a mixture of gelatin (10% wt.) and sucrose (7.5% wt.). Cryosectioning was performed with a cryostate (Leica, Germany) at 10 μm. Tissue sections were stained with hemotoxylin and eosin (H&E) for histological assessment. For immunofluorescent staning, section were blocked and permeabilized in BSA (1% wt.) and 0.25% Triton-X, respectively. Sections were then incubated

with primary antibodies Nestin (invitrogen MA1-110), βIII-Tubulin (santa cruz sc-51670), and SATB2 (invitrogen PA5-20533). Secondary andibodies used were goat anti-mouse IgG (Alexa Fluor 488, Thermo Fisher, A-11008) and goat anti-rabbit IgG (Alexa Fluor 568, Thermo Fisher A-11011) IgG. Nuclei were stained with DAPI. Microscopic observation was performed under an epifluorescent microscope (Leica DMIL model, Leica, Germany).

2.7. Transcriptome analysis

To reveal the transcriptomic similarity and difference in COs grown in **HA-Tyr(1%)/IKVAV-PA** and Matrigel, we performed a transcriptomics analyses using RNA-seq by NovaSeq 6000 (Illumina, USA). COs grown in **HA-Tyr(1%)** were used as negative control, while COs grown in **HA-Tyr(3%)/IKVAV-PA** were used to reveal the effect of matrix stiffness on the transcript profile of COs. The procedure for pooling organoids to make 30 organoids per sample and a sufficient amount of RNA as described in the gene expression analysis was exactly followed in the transcriptomics analysis. We extracted the RNA with the RNeasy mini kit (Qiagen, USA). Messenger RNA was purified from total RNA using poly-T oligo-attached magnetic beads. Raw data of FASTQ format were first processed through an in-house perl scripts. In this step, clean data were obtained by removing reads containing adapter, reads containing poly-N and low quality reads.

2.8. Proteome analysis

To investigate the effect of matrix bioactivity and stiffness on the proteomic structure of COs, COs grown in **HA-Tyr(1%)**, **HA-Tyr(1%)/IKVAV-PA**, **HA-Tyr(3%)/IKVAV-PA**, and Matrigel were taken out by digesting the gels with hyaluronidase. Organoid-pooling procedure as detailed in the previous sections was followed to obtain sufficient amount of protein. COs were treated with methanol/water mixture (9:1, v/v), and protein pellets were re-dissolved with ammonium bicarbonate (100 mM) containing 20% methanol. An equal quantity of protein from each sample was used, thereby, the biological variance across samples was normalized. The samples then were vortexed and reduced with dithiothreitol (DTT, 50mM) for 30 min at 56 °C. Samples were then cooled down to room temperature and treated with 100mMiodoacetamide (IAA) in the dark at room temperature for 30 min. The reduced and alkylated protein samples were digested with trypsin (1:30 w/w) for 4h at 37°C. Next, the samples were evaporated to dryness and diluted in 0.1% formic acid (FA) containing water/acetonitrile solution.

Proteomic analyses were performed using LC-qTOF-MS with a C18 column (150 × 1 mm, 5 μm, 300 Å, Phenomenex Jupiter, USA). Agilent MassHunter Workstation Software Q-TOF B.08.00 was used to run the Agilent 1260 Infinity series LC and 6530 accurate-mass LC–qTOF-MS instrument in auto MS/MS positive ionization mode. The MS/MS scan data were collected in the *m*/*z* range of 100–1700. Reference mass correction was achieved using tuning mix (Agilent 85000 ESI-TOF Tuning Mix, Agilent, USA).

2.9. Metabolome analysis

Metabolomic analyses were performed to reveal the possible metabolic differences in COs grown in **HA-Tyr(1%)**, **HA-Tyr(1%)/IKVAV-PA**, **HA-Tyr(3%)/IKVAV-PA**, and Matrigel. Metabolomics analyses have been adopted from our previous studies [22,38]. Briefly, metabolites extracted from COs (30 COs per sample) by treating with methanol: water mixture (9:1, v/v, 1 mL). Normalisation was achieved as described in the proteome analysis. The samples were transferred into Eppendorf tubes and vortexed and centrifuged at 10000 rpm for 10 min. Two aliquots containing 200 µL supernatant from each sample were completely dried in vacuum concentrator. Finally, the samples were analysed by gas chromatography-mass spectrometry (GC-MS) and liquid chromatography-quadrupole time of flight-mass spectrometry (LC-qTOF-MS).

GC-MS based metabolomic analyses: The dried samples were methoxylated using methoxyamine hydrochloride in pyridine (20 mg mL^{-1}) for 90 min at 30°C. Shortly after, the samples were derivatized using *N*-methyl-*N*-trimethylsilyl trifluoroacetamide (MSTFA) and trimethylchlorosilane (TMCS, 1%) for 30 min at 37°C. Samples transferred to silylated vials were analyzed by GC-MS system (GC-MS-QP-2010 Ultra system, Shimadzu, Japan) with a DB5-MS column (30 m +10 m duraguard × 0.25 mm i.d. and 0.25-µm film thickness). The run time and injection volume were set at 37.5 min and 1 µL (splitless), respectively. The MS scan data were collected in the range of 50–650 m/z using GC-MS Solution (Shimadzu, ver. 4.20). Injection temperature and the flow rate were set at 290°C and 0.99 mL min^{-1}, respectively. The solvent delay time was adjusted to 5.90 min.

LC-qTOF-MS based metabolomic analyses: The dried samples were diluted with water and acetonitrile (both containing 0.1% FA) mixture (1:1, v/v). Then, the samples were transferred to vials and analyzed using LC–qTOF-MS system (Agilent 6530 accurate-mass, Santa Clara, USA) operated with an electrospray ion source (ESI) in positive and negative ionization mode. Chromatographic separation was performed using C18 column (2.1 x 100 mm, 2.7 µm) with a

mobile phase of 0.1% FA containing water (A) and 0.1% FA containing acetonitrile (B) with gradient elution (0–1 min, 10% B, 1–14 min 10−90% B, 14–15 90% B, 15–20 min 90–10%, 20–25 90-10% B). The flow rate was set at 0.3 mL min^{-1} and injection volume was 20 µL. Capillary voltage and gas temperature was adjusted to 3500 V and 300 °C, respectively. The MS scan data were acquired in the range of m/z 100–1700 using Mass Hunter Data Acquisition B.08.00 (Agilent, USA). The QC samples were analyzed in targeted MS\MS mode at 10, 20 and 40 eV for a reliable identification.

2.10. Statistical analysis and bioinformatics

Transcriptomics data analysis: Differential expression analysis (DEA) of two-group comparisons (two biological replicates per condition) was performed using the DESeq2 R package (1.20.0). The resulting *p*-values were adjusted using the Benjamini and Hochberg's approach for controlling the false discovery rate. Genes with an adjusted *p*-value <0.05 found were assigned as differentially expressed. Gene Ontology (GO) enrichment analysis of differentially expressed genes was implemented by the cluster Profiler R package.

Proteomics data analysis: The "label-free quantification" algorithm (MAX-LFQ) was utilized to determine the intensities of proteins that differed across experimental groups. The FAST-LFQ algorithm, which is embodied in the Max-LFQ algorithm, was used to normalize the data set. Following MAX-LFQ analysis, the normalized dataset was evaluated with Perseus, and "contaminants", "reverse" and "only identified by site" matched proteins were filtered. Following that, the normalized data were logarithmized using the log2(x) transformation to improve the data's behavior in statistical tests, and it was determined that the data were normally distributed before performing statistical analysis.

Metabolomics data analysis: Deconvolution, peak alignment and metabolite identification were carried out with MS-DIAL (ver. 4.48) software for both metabolomic data. The peak annotations were done using retention index libraries for GC-MS analysis. For LC-MS based metabolomic analysis, high-resolution MS systems like TOF are required in untargeted metabolomics analysis for metabolite identification. However, a second orthogonal data is necessary for precise metabolite annotations. This data can be obtained by either matching with the retention time of standard or mass fragmentation pattern (MS/MS spectrum) using tandem mass spectrometry like qTOF-MS system. In the study, high-resolution mass spectrum (MS1) and MS/MS spectrum (MS2) data were used for formula predictions, and structure elucidations

by means of unknown spectra by querying the acquired MS2 data against the Human Metabolome Database (HMDB), Lipid Maps, Chemical Entities of Biological Interest (ChEBI) and PubChem with MS-Finder (ver. 3.50) software. TIC normalization was done for raw data set and mean scaling was applied to identified metabolite list in each group. Statistical analysis was carried out in Metaboanalyst 5.0 and 50% of the values missing were excluded from the data matrix, and PLS-DA, heatmap, one-way ANOVA, volcano, pathway impact plots were created.

3. Results and Discussion

3.1. Rationale of design

It is well-known that the bioactivity and stiffness of the ECM can have significant effects on cell behavior and tissue formation. Therefore, we aimed to modulate brain organoid development across multiple length scales using a 3D matrix that presents bio-instructive epitopes, mechanical cues, and nanoscale architecture that resemble those from the native ECM. To do so, we developed a hybrid nanofibrous hydrogel with the capacity to present iPSCs cells with both a neuro-inductive epitope and tunable stiffness. We designed a cationic PA with the sequence C16-V3A3K3IKVAV bearing the laminin-derived amino acid sequence (IKVAV, Ile-Lys-Val-Ala-Val) (**Figure 1A**) known to promote neurogenesis [39]. To modulate hydrogel stiffness, we electrostatically co-assembled this IKVAV-PA with a negatively charged tyramine-modified hyaluronic acid (HA-Tyr, **Figure 1A**). HA-Tyr backbone presents carboxylate groups able to electrostatically interact with the lysine-based cationic PAs (**Figure 1B**) [40]. In addition, oxidative coupling of the co-assembled structures mediated by H_2O_2/HRP system enables the formation of self-supporting hydrogels in a HA-Tyr concentration-dependent manner. Given the limitations associated with the use Matrigel to grow brain organoids [10], here we demonstrate the use of our HA-Tyr/IKVAV-PA matrix as an alternative to induce EBs towards cerebral organoids.

3.2. Synthesis of laminin-mimetic PAs and characterization of HA-Tyr/PA hydrogels

We synthesized PAs bearing a laminin-derived sequence (PA-IKVAV; $C_{16}H_{31}$CONH-V3A3K3IKVAV) as well as the scrambled analogue (PA-VKIVA; $C_{16}H_{31}$CONH-V3A3K3VKIVA) (**Figure 1A**) using a solid-phase peptide synthesis approach and purified as previously reported [19,20,22,23]. Zeta potential measurements showed that both PA-IKVAV

(ζ = +12.3 mV) and PA-VKIVA (ζ = +12.7 mV) are highly positively charge, suggesting the possibility to electrostatically co-assemble with an anionic HA-Tyr (ζ = - 31.1 mV) (**Figure 1B**). TEM micrographs revealed the capacity of the PAs to self-assemble into cylindrical nanofibers with 10 nm in diameters and several microns long in length while circular dichroism (CD) spectroscopy showed that the PAs displayed a β-sheet conformation when dissolved in an aqueous media [41] **(Figure 1C, D**).

We created hydrogels with tunable physico-mechanical properties by using various concentrations of HA-Tyr (1 and 3 % wt.). Hydrogels synthesis was carried out by H_2O_2 (2 mM)/horse-radish peroxidase (HRP)-mediated oxidative coupling. Hydrogels were created with and without IKVAV-PA (1 % wt.). To create HA-Tyr/IKVAV-PA hybrid hydrogels, we co-assembled an anionic HA-Tyr (1% wt. or 3% wt.) with cationic PAs (**Figure 1E**). Then we chemically crosslinked the preformed structures via H_2O_2/HRP mediated oxidative coupling. We used dynamic oscillatory rheology to assess the mechanical properties of HA-Tyr hydrogels with and without PAs. The frequency sweep rheographs for HA-Tyr (1% wt.), HA-Tyr (1% wt.)/PA(1% wt.), HA-Tyr (3%), and HA-Tyr (3% wt)/PA (1% wt.) showed that the the storage modulus G' (elastic component) is greater than the loss modulus G" (viscous component) and that both G' and G" are frequency independent, indicating that the hydrogels are visco-elastic in nature (**Figure 1F**, S**upplementary Figure S1 – S4**). When we increased the concentration of HA-Tyr from 1 to 3 % wt, the G' value (stiffness) increases from 0.69 to 2.24 kPa. Similarly, the incorporation of 1% wt of PAs into the hydrogels increases the stiffness of HA-Tyr (1% wt.) and HA-Tyr (3% wt.) to 0.91 and 3.07 kPa, respectively. Thus, suggesting that the electrostatic interactions between the cationic PAs nanofibers and anionic HA-Tyr also contributes to stiffness enhancement. Using scanning electron microscopy, we confirmed that hydrogels developed with HA-Tyr (1% wt.) displayed porous microstructures when compared with HA-Tyr (3% wt.) hydrogels, which were not only less porous but also showed collapsed microstructures as a result of high crosslinking density (**Figure 1G**). This morphological differences might explain the observed difference in the mechanical property of HA-Tyr(1% wt.) and HA-Tyr(3% wt.). As expected, HA-Tyr/PA hydrogels exhibited the classical nanofibrillar architecture (**Figure 1H**). In addition, the suitability of the resulting HA-Tyr/IKVAV-PA hydrogels in long-term cell culture applications was tested by a degradation study. We observed that both HA-Tyr(1%)/IKVAV-PA and HA-Tyr(3%)/IKVAV-PA preserved almost 70% of their initial weight up to 28-days of incubation (**Figure S5**), which is sufficient for a long-term culture and organoid induction.

3.3. Cytocompatibility of hydrogels

To assess the suitability of the hydrogels as a 3D culture matrix for brain organoids, we then performed viability and proliferation tests on hNSCs encapsulated in various hydrogels including HA-Tyr (1 and 3%) as well as HA-Tyr/IKVAV-PA with various PA concentrations (0.1, 1, 2% wt.). Inverted microscope images depicted hNSCs forming spheroidal structures within HA-Tyr(1%) and smaller ones in HA-Tyr(3%) after 2 days of culture (**Figure S6A**), which is a morphology known to be crucial for organoid formation. However, there was no significant difference in the cell viability and proliferation capability of cells in HA-Tyr(1%) and HA-Tyr(3%) (**Figure S6B**). The cells also formed small spheroids and showed good viability and proliferation in HA-Tyr/IKVAV-PA hydrogels prepared with various concentrations of PAs (0.1, 1, and 2%) until day 2 in culture, however, the cells embedded in hydrogels prepared with 2% PAs displayed low cell viability and inhibition of cell proliferation (**Figure S6C**). Therefore, unless otherwise specified, IKVAV-PA (1%) was used throughout the work.

Figure 1

3.4. Organoid culture in HA-Tyr/PAs hydrogels

The conventional protocol to generate brain organoids involves a few consecutive steps including induction of hPSCs into EBs in ULAP, induction of EBs towards neuroepithelial tissue, embedment and culture of the tissue in Matrigel with an expansion medium, and final culture in maturation medium to obtain functional organoids (**Figure S7A**). Our approach presents a shorter and simpler process to embed EBs and further induce cerebral organoids (**Figure S7B**). After 4 days of neural induction in HA-Tyr/IKVAV-PA, the EBs displayed a brighter structure on the edges and a dense core as expected (**Figure 2A**). Following the neural induction, expansion, and maturation processes in HA-Tyr/IKVAV-PA, the EBs formed COs with irregular morphology and multiple buddings similar to the COs obtained in Matrigel with the conventional protocol (**Figure 2A**). This observation is in consonance with a previous report that reports the ability of fibrous morphologies to improve forebrain identity [15]. The EBs in HA-Tyr hydrogels preserved their smooth-edged structure after incubation in neural induction and expansion media. The inability of EBs to form the classical irregular and expanded structures of COs under this condition might be attributed to the inert, hydrophilic, and non-fibrous architecture of HA-Tyr hydrogels. In contrast, EBs cultured in HA-Tyr/VKIVA-PA

hydrogels, formed an irregular but budding-poor structures. This resulting structure is thought to be due to the inert but fibrous structure of HA-Tyr/VKIVA-PA. These results demonstrate that the nanofibrous structure of PAs results in morphologic difference in EBs, however, the bioactivity of PAs is the key to induce EBs into COs transition.

Figure 2

We also investigated the effect of matrix bioactivity on organoid formation in various hydrogels via gene expression analyses. To this end, the expressions of Nestin, PAX6, TUJ1, MAP2, FOXG1, and SATB2 were assessed in COs in comparison to EBs, which were grown in HA-Tyr(1%), HA-Tyr(1%)/IKVAV-PA, HA-Tyr(1%)/VKIVA-PA, and Matrigel. We observed a significantly higher expression of Nestin and PAX6, two neural stem cell markers, in COs grown in HA-Tyr hydrogels relative to the COs grown in HA-Tyr(1%)/IKVAV-PA hydrogels and Matrigel (**Figure S8**). The upregulated expression of these two neural stem cell markers in HA-Tyr/IKVAV-PA hydrogels over HA-Tyr hydrogels might be attributed to the inert nature of HA-Tyr without PAs, which is not able to provide the required niche for tissue specification [42] and neuroepithelial tissue development for further induction towards neuronal cells. On the other hand, there was no significant difference in the expressions of Nestin and PAX6 in HA-Tyr(1%) and HA-Tyr(1%)/VKIVA-PA hydrogels (**Figure S8**). In contrast, the expressions of TUJ1 and MAP2, two neuronal markers, were seen to be upregulated in COs grown in HA-Tyr(1%)/IKVAV-PA hydrogels and Matrigel compared to HA-Tyr(1%) and HA-Tyr(1%)/VKIVA-PA, which suggests that the bioactivity of PAs plays a critical role in organoid induction. Also, we examined the expression of FOXG1 and SATB2, two cortical markers, by COs embedded in various hydrogels to further assess organoid induction and maturation. We found that COs grown in HA-Tyr(1%)/IKVAV-PA hydrogels and Matrigel showed an up-regulated expression of FOXG1 and SATB2 when compared to HA-Tyr(1%) and HA-Tyr(1%)/VKIVA-PA. There was no significant differences between the expression of FOXG1 and SATB2 in HA-Tyr(1%)/IKVAV-PA hydrogels and Matrigel, implying that both matrices support an effective neuronal induction and organoid expansion. These findings enable us to conclude that the emerging organoids exhibit SVZ and forebrain identities. It should also be noted that the expressions of these genes were relatively low when compared to NSC/neuronal markers, which might be due to the short maturation period (4 days) used in our work. This period can be extended to months depending on the purpose of the ultimate function [43]. These results demonstrate that EBs in HA-Tyr-based hydrogels can induced into neuroepithelial tissue

that is enriched with neural stem cells, however, further neuronal induction requires the bioactivity of PAs.

To corroborate the gene expression study, we also performed histology and immunofluorescent imaging. H&E staining provided an overall histological image of COs grown in HA-Tyr(1% wt.), HA-Tyr/IKVAV-PA, and Matrigel (**Figure 2B**). COs grown in HA-Tyr/IKVAV-PA and Matrigel exhibited a classical histology of COs with buddings and ventricles (shown by arrows), while in HA-Tyr, COs failed to form proper ventricles and yielded distorted structures (shown by stars). To provide a more detailed information and determine the type of cells that COs have, we performed an immunostaining with Nestin (neural stem cell marker), βIII-Tubulin (neuronal marker), and SATB2 (late-born neuronal marker). COs grown in HA-Tyr and Matrigel exhibited Nestin+ βIII-Tubulin+ image, proving that the COs grown in these matrices have both ventricular neural stem cells and neurons (**Figure 2C**). Furthermore, COs grown in HA-Tyr/IKVAV and Matrigel have a limited level of SATB2+ cells that show the superficial neuronal identity. Yet, the number of these cells were higher in COs grown in Matrigel as compared to HA-Tyr/IKVAV-PA. On the other hand, COs grown in HA-Tyr exhibited a Nestin+βIII-Tubulin- SATB2- structure, implying that tissues grown in this matrix highly bear neural stem cells, but neurons. All these observations through immunofluorescent imaging highly overlap with the data obtained by gene expression analysis, and confirm that COs grown in HA-Tyr/IKVAV-PA display a similar character with that grown in Matrigel. Also, the presence of bioactive PAs is crucial in the neuronal induction.

3.5. Transcriptome analysis

We hypothesized that matrix bioactivity and stiffness would modulate the biomolecular structure of organoids. To test this hypothesis, we first performed a transcript profiling in COs which were grown in HA-Tyr(1%), HA-Tyr(1%)/IKVAV-PA, HA-Tyr(3%)/IKVAV-PA, and Matrigel. The whole structure of COs grown in HA-Tyr/IKVAV-PA and Matrigel were presented in **Figure 3A** to give an understanding of the relation of histological structures of COs with their molecular profiles. Principle component analysis (PCA) revealed a clear discrimination in the transcriptome of COs grown in each matrix (**Figure 3B**). The expression pattern of all individual genes was presented in the heat-map diagram with hierarchical clustering analysis (**Figure 3C**). Pearson correlation analysis indicated that the correlations in the transcriptomic structure between HA-Tyr(1%) and Matrigel (~0.3) as well as between HA-

Tyr(1%) and HA-Tyr(1%)/IKVAV-PA (~0.6) were weak (**Figure 3D**), which is a due to the absence of PAs. It should also be noted that, in-group correlation in the transcriptomic structure of COs grown in Matrigel was not high (0.65), which is attributed to its poorly-defined biochemical content of Matrigel. This heterogeneous structure of Matrigel may lead variation in organoid formation yield and inhomogeneous molecular structure of the yielding organoids. On the other hand, a correlation in the transcriptome was observed between Matrigel and PA-based matrices. The correlation between HA-Tyr/PA and Matrigel was performed by comparing the average gene expressions of each group, which resulted in correlations between HA-Tyr(1%)/PA and Matrigel to be 0.73 and between HA-Tyr(3%)/PA and Matrigel to be 0.78. The number of transcripts differentially expressed or shared across groups –which were obtained by the median of each group– was presented in the Venn scheme (**Figure 3E**). These results demonstrate that PAs are the key in guiding organoid induction, and resulting organoids exhibit a similar transcriptomic structure to those obtained with Matrigel.

To investigate the effect of IKVAV-PA-mediated bioactivity on the transcript profiles of COs, we compared transcriptomes of COs grown in HA-Tyr(1%)/IKVAV-PA and HA-Tyr(1%) hydrogels, as well as in HA-Tyr(1%)/IKVAV-PA hydrogels and Matrigel. We identified 1717 up-regulated and 480 down-regulated transcripts in the comparison of HA-Tyr(1%)/IKVAV-PA and HA-Tyr(1%) hydrogels (**Figure S9**). The roles of 25 differentially up-regulated genes with the least *p*-values (p=0.0001-0.00035) on neurogenesis were assessed (**Table S1**). For example, one of the most significant differentially expressed genes -LARGE2- between HA-Tyr(1%)/IKVAV-PA and HA-Tyr(1%) hydrogels play a critical role in laminin-binding. It has been previously reported that the hyperglycosylated proteins in LARGE-overexpressing cells showed a functional capacity to bind the extracellular matrix molecule laminin [44], which perfectly fits with our approach, given that our IKVAV-PA can mimic the functional property of ECM laminin. Similarly, the roles of other up-regulated genes (HES7, EGR1, CDC25B, and NOP2) (**Figure 3F**) in neurogenesis and NSC differentiation have been extensively reported [45-49], which also supports our findings on Nestin+PAX6+ COs revealed by RT-qPCR (**Figure S8**). Moreover, up-regulation of some forebrain-related transcripts, i.e., HOXA13, FOXM1, and FZD9 (**SI Excel I**), well overlaps with FOXG1+SATB2+ COs as determined by RT-qPCR (**Figure S4**). It is noteworthy that a large number of genes were not significantly up- or down-regulated in the transcriptome of COs grown in HA-Tyr(1%)/IKVAV-PA hydrogels compared to COs grown in Matrigel (**Figure S9**). Interestingly, a set of genes including LAM1A1, LAMB3, LAMC2, NGF, VCF, ENC1, NEDD1, NEDD4, NEURL2, MTURN,

NPDC1, ATRAID, NEURDD2 responsible for stem cell differentiation and neurogenesis were regulated to a similar degree in our HA-Tyr(1%)/IKVAV-PA hydrogels and Matrigel (**Figure 3G**). In light of these results, we conclude that IKVAV-PA is a key instructive component to induce neuroepithelial tissue towards COs formation.

Figure 3

GO analysis of significantly up-regulated genes (LARGE2, KRT16, EXD3, HIST1H2, amongst others) in COs grown in HA-Tyr(1%)/IKVAV-PA also revealed the enrichment of protein and nucleic acid-based functions as well as molecular functions including laminin binding, ECM binding, and ECM structural constitution (**Figure 4Ai**). These effects lend credence to our previous findings on the differentially expressed genes between the tested groups. Comparing HA-Tyr(1%)/PA-IKVAV and Matrigel, up-regulated genes including CHI3L1, CFAP157, UNC5A, amongst others in COs resulted in the enrichment of mostly transmembrane activities such as sodium channel activity and cation transmembrane transport activity, which are related to the maturation phase of COs (**Figure 4Aii**).

Figure 4

We also compared the differentially expressed genes (DEGs) in COs grown in HA-Tyr(1%)/IKVAV-PA and HA-Tyr(3%)/IKVAV-PA to reveal the affected pathways by altering matrix stiffness. A big part of the genes were shared between the two groups, and only 167 genes were seen to be up-regulated in COs grown in HA-Tyr(1%)/IKVAV-PA hydrogels (**Figure S9**). The DEGs ($p<0.05$, **Table S2**) were mostly related to protein localization process and matrix stiffness-related molecular functions such as cell adhesion molecule binding and cadherin binding, which were enriched in COs grown in HA-Tyr(1%)/IKVAV-PA hydrogels (**Figure 4B**).

3.6. Proteome analysis

To further corroborate the effects of matrix bioactivity and stiffness on the biomolecular structure of COs, we performed an untargeted proteomics analysis for COs grown in HA-Tyr(1%)/IKVAV-PA and HA-Tyr(1%) hydrogels as well as HA-Tyr(1%)/IKVAV-PA hydrogels and Matrigel. The PCA revealed a clear discrimination in the proteome of COs grown in HA-Tyr(1%)/IKVAV-PA and HA-Tyr(1%) hydrogels (**Figure 5A**). This discrimination was further confirmed by the Biplot diagram (**Figure 5B, SI Excel IV**), which shows the compositional difference between the groups and indicates their negative correlation. A

heatmap of protein translation changes indicated that more proteins were up-regulated in COs grown in HA-Tyr(1%)/IKVAV-PA hydrogels compared to COs in HA-Tyr(1%) hydrogels (**Figure 5C**). The list of the 25 most up-regulated proteins is provided in **Table S3**. Importantly, some of the positively correlated proteins in COs grown in HA-Tyr(1%)/IKVAV-PA hydrogels were seen to be directly related to neural cell adhesion (laminin subunit alpha 3 and 5, beta 2, protocadherin 23, actin cytoplasmic 1, actin-binding protein anillin), differentiation (tubulin alpha 1A, 4A, laminin subunit alpha 3 and 5, laminin subunit beta 2) (**Figure 5D, SI Excel IV)**, which correlate with the transcriptome data. Comparing HA-Tyr(1%)/IKVAV-PA hydrogels and Matrigel, the discrimination shown in PCA (**Figure 5E**) was ordinary as confirmed by Biplot diagram (**Figure 5F, SI Excel IV**). It is noteworthy that, a large part of the proteins was located and accumulated between two groups as seen in the Biplot diagram, highlighting that there was a positive correlation between the groups. The proteins that formed a pattern transition and clustering as observed in the heatmap (**Figure 5G, Table S4**) were not directly associated with neural cell adhesion or differentiation. Also, the discriminated and differentially expressed proteins were not statistically significant ($p<0.05$, fold change>2) as confirmed by the Volcano plot (**Figure 5H**). Overall, it can be concluded that IKVAV-PAs play a significant role in the neural specification of organoids, and lead to a similar proteomic signature with the gold standard Matrigel.

Figure 5

To reveal the proteomic signature of matrix stiffness in COs, we compared the proteome of COs grown in HA-Tyr(1%)/IKVAV-PA and HA-Tyr(3%)/IKVAV-PA hydrogels. In this case, we observed a clear discrimination between groups (**Figure 6A**) and the proteins were seen to accumulate away from the opposite group (**Figure 6B, SI Excel IV**), meaning that those proteins were not regulated to a similar level. The differentially expressed proteins (**Table S6**) formed a large cluster of proteins in the heatmap diagram that were up-regulated in HA-Tyr(1%)/IKVAV-PA hydrogels and down-regulated in HA-Tyr(3%)/IKVAV-PA hydrogels (**Figure 6C**). Strikingly, there seemed to be an up-regulation in cell adhesion-related proteins, such as actin cytoplasmic 1, and dynein heavy chain 2, 7, 17, and down-regulation in tubulin in COs grown in HA-Tyr(3%)/IKVAV-PA hydrogels (**Figure 6D**), implying that matrix stiffness could have a significant effect on the proteomic structure of COs.

Figure 6

3.7. Metabolome analysis

In addition to transcriptome and proteome analyses, we further carried out a high-throughput metabolomics analysis, which is able to provide information on the ultimate state of the biomolecular cascades (<1,500 Da). We first compared the metabolome of COs grown in HA-Tyr(1%)/IKVAV-PA hydrogels and HA-Tyr to reveal the effects of matrix bioactivity on organoid metabolism. PLS-DA plot showed the variance in the metabolic structures between HA-Tyr(1%)/IKVAV-PA hydrogels and HA-Tyr (**Figure 7A**). The hierarchical clustering of metabolites for COs that significantly changed in HA-Tyr(1%)/IKVAV-PA hydrogels and HA-Tyr is provided in **Figure 7B**. Differentially expressed metabolites identified in COs grown in HA-Tyr(1%)/IKVAV-PA hydrogels were highlighted in the coefficient plot (**Figure 7C**). Enriched metabolic pathways obtained by the most differentially regulated metabolites revealed that glutathione metabolism and glyoxylate and dicarboxylate metabolism pathways were the main pathways affected by the matrix biological activity, i.e. PAs (**Figure 7D**). We then elucidated the metabolomic difference in COs that were grown in HA-Tyr(1%)/IKVAV-PA hydrogels and Matrigel. The PLS-DA showed discrimination in the metabolome between HA-Tyr(1%)/IKVAV-PA and Matrigel groups (**Figure 7E**); the alteration in metabolite levels has been observed a wider distribution in this case (**Figure 7F**). A total of 103 metabolites were identified, however, only 4 up-regulated (4-hydroxyphenylacetic acid, LysoPE, LysoPC, L-isoleucine) and one down-regulated (oleamide) metabolites were found to be statistically significant (*$p<0.05$, fold change>2*) (**Figure 7G**). These results further corroborate the biomolecular similarity in COs grown in HA-Tyr/IKVAV-PA hydrogels and the gold standard Matrigel.

Figure 7

It is well known that cell metabolism is affected by both matrix bioactivity and stiffness [50]. To reveal the effects of HA-Tyr/IKVAV-PA hydrogel stiffness on the metabolism of COs, we repeated metabolite profiling for COs that were grown in HA-Tyr(1%)/IKVAV-PA hydrogels and HA-Tyr(3%)/IKVAV-PA. A substantial difference in the metabolite profiles of COs was seen with the altered matrix stiffness as confirmed by the PLS-DA diagram (**Figure 8A**) and heatmap with hierarchical cluster analysis (**Figure 8B**). Polyunsaturated fatty acids (e.g., diacylglycerophosphoserine (PS(22:4(7Z, 10Z, 13Z))), docosapentaenoic acid, LysoPC(14:0), linoleamide) and amino acids (e.g., isoleucine, 5-hydroxytriptophane, alanine, tyrosine, glycine) were dominant across up-regulated metabolites (**Figure 8C**). In addition to amino acid anabolic pathways, glutathione and glycerophospholipid metabolism pathways were found to be the main pathways affected by the up-regulated metabolites, as illustrated by the pathway

enrichment graph (**Figure 8D**). Previous studies [51,52] have reported that polyunsaturated fatty acids regulate cell survival, neurogenesis, and synaptic function, evidenced by an increase in levels of diacylglycerophosphoserine in neurons [53]. Our findings demonstrate an increase in the level of polyunsaturated fatty acids in COs grown in the soft hydrogel, indicating a higher level of neuronal differentiation and maturation. This result aligns with previous studies reporting regulation of stem cells and neural cells in favor of neurogenesis through lipid-based mechanisms [54,55] and close relationships between matrix stiffness and amino acid metabolism [56].

Figure 8

4. Conclusion

Hybridization of self-assembling peptides and ECM-derived polymer offers an attractive strategy to develop biocompatible, bio-instructive, nanofibrous, and mechanically tunable matrices for organoids technology. Here, we developed two-component hydrogel materials that integrates the nanofibrous architecture and neuro-instructive activity of laminin-mimetic peptide amphiphiles and tunable stiffness of HA-Tyr to induce and grow cerebral organoids. We harnessed a broad range of high-throughput screening techniques including transcriptomics, proteomics, and metabolomics, to reveal the effects of matrix stiffness and presentation of neuro-inductive cues in HA-Tyr/IKVAV-PA hydrogels on the induction of pluripotent stem cells towards cerebral organoids. The multi-omics techniques reveal that the stiffness, nanofiber architecture and neuro-inductive cues of our HA-Tyr/IKVAV-PA hydrogels synergistically modulate the biomolecular plasticity and morphological transformation of COs grown therein to the same magnitude observed in Matrigel. Thus, suggesting our hydrogels hold great potential as attractive substitutes for the animal-derived Matrigel. This study also showed that both matrix stiffness, nanoscale architecture and bio-instructive cues have significant effect on the histogenesis of cerebral organoids, providing fundamental insight into the roles of ECM parameters on organoids induction and growth. Notwithstanding, the possibility to create tunable hydrogels incorporating multiple PAs bearing epitopes derived from essential ECM components will enable us to recapitulate the complexity of the native organ in the future. Such improved design strategy will help us to identify optimum matrix parameters to effectively create cerebral organoids.

Acknowledgement

This work was financially supported by the Turkish Scientific and Technological Research Council (TUBITAK, grant no: 119S363) as well as the Medical Research Council (UK Regenerative Medicine Platform Acellular/Smart Materials 3D Architecture, MR/R015651/1. BOO thanks the University of Nottingham for the award of Nottingham Research Fellowship.

References

1. M. Eiraku, K. Watanabe, M. Matsuo-Takasaki, M. Kawada, S. Yonemura, M. Matsumura, T. Wataya, A. Nishiyama, K. Muguruma, Y. Sasai, Self-organized formation of polarized cortical tissues from escs and its active manipulation by extrinsic signals, Cell Stem Cell. 3 (2008) 519–532. doi:10.1016/j.stem.2008.09.002.

2. T.A. Longmire, L. Ikonomou, F. Hawkins, C. Christodoulou, Y. Cao, J.C. Jean, L.W. Kwok, H. Mou, J. Rajagopal, S. Shen, A.A. Dowton, M. Serra, D.J. Weiss, M.D. Green, H-W. Snoeck, M.I. Ramirez, D.N. Kotton. Efficient derivation of purified lung and thyroid progenitors from Embryonic Stem Cells, Cell Stem Cell. 10 (2012) 398–411. doi:10.1016/j.stem.2012.01.019.

3. K.W. McCracken, E.M. Catá, C.M. Crawford, K.L. Sinagoga, M. Schumacher, B.E. Rockich, Y-H. Tsai, C.N. Mayhew, J.R. Spence, Y. Zavros, J.M. Wells, Modelling human development and disease in pluripotent stem-cell-derived gastric organoids, Nature. 516 (2014) 400–404. doi:10.1038/nature13863.

4. S.-I. Mae, A. Shono, F. Shiota, T. Yasuno, M. Kajiwara, N. Gotoda-Nishimura, S. Arai, A. Sato-Otubu, T. Toyoda, K. Takahashi, N. Nakayama, C.A. Cowan, T. Aoi, S. Ogawa, A.P. McMahon, S. Yamanaka, K. Osafune. Monitoring and robust induction of nephrogenic intermediate mesoderm from human pluripotent stem cells, Nature Communications. 4 (2013). doi:10.1038/ncomms2378.

5. T. Takebe, K. Sekine, M. Enomura, H. Koike, M. Kimura, T. Ogaeri, R-R. Zhang, Y. Ueno, Y-W. Zheng, N. Koike, S. Aoyama, Y. Adachi, H. Taniguchi. Vascularized and functional human liver from an IPSC-derived organ bud transplant, Nature. 499 (2013) 481–484. doi:10.1038/nature12271.

6. J.R. Spence, C.N. Mayhew, S.A. Rankin, M.F. Kuhar, J.E. Vallance, K. Tolle, E.E: Hoskins, V.V. Kalinichenko, S.I. Wells, A.M. Zorn, N.F. Shroyer, J.M. Wells. Directed

differentiation of human pluripotent stem cells into intestinal tissue in vitro, Nature. 470 (2010) 105–109. doi:10.1038/nature09691.

7. H. Suga, T. Kadoshima, M. Minaguchi, M. Ohgushi, M. Soen, T. Nakano, N. Takata, T. Wataya, K. Muguruma, H. Miyoshi, S. Yonemura, Y. Oiso, Y. Sasai. Self-formation of functional adenohypophysis in three-dimensional culture, Nature. 480 (2011) 57–62. doi:10.1038/nature10637.

8. H. Sakaguchi, T. Kadoshima, M. Soen, N. Narii, Y. Ishida, M. Ohgushi, J. Takahashi, M. Eiraku, Y. Sasai, Generation of functional hippocampal neurons from self-organizing human embryonic stem cell-derived dorsomedial telencephalic tissue, Nature Communications. 6 (2015). doi:10.1038/ncomms9896.

9. K. Muguruma, A. Nishiyama, H. Kawakami, K. Hashimoto, Y. Sasai, Self-organization of polarized cerebellar tissue in 3D culture of human pluripotent stem cells, Cell Reports. 10 (2015) 537–550. doi:10.1016/j.celrep.2014.12.051.

10. M.A. Lancaster, J.A. Knoblich, Generation of cerebral organoids from human pluripotent stem cells, Nature Protocols. 9 (2014) 2329–2340. doi:10.1038/nprot.2014.158.

11. H. Poudel, K. Sanford, P.K. Szwedo, R. Pathak, A. Ghosh. Synthetic matrices for intestinal organoids: Implication for better performance. ACS Omega. 7 (2022) 38-47. doi.org/10.1021/acsomega.1c05136

12. E.A. Aisenbrey, W.L. Murphy, Synthetic Alternatives to matrigel, Nature Reviews Materials. 5 (2020) 539–551. doi:10.1038/s41578-020-0199-8.

13. Broguiere, N., Isenmann, L., Hirt, C., Ringel, T., Placzek, S., Cavalli, E., Ringnalda, F., Villiger, L., Züllig, R., Lehmann, R., Rogler, G., Heim, M.H., Schüler, J., Zenobi-Wong, M., G. Schwank. Growth of epithelial organoids in a defined hydrogel, Advanced Materials. 30 (2018) 1801621. doi:10.1002/adma.201801621.

14. R. Cruz-Acuña, M. Quirós, A.E. Farkas, P.H. Dedhia, S. Huang, D. Siuda, V. Garcia-Hernandez, A.J. Miller, J.R. Spence, A. Nusrat, A.J. Garcia. Synthetic hydrogels for human intestinal organoid generation and colonic wound repair, Nature Cell Biology. 19 (2017) 1326–1335. doi:10.1038/ncb3632.

15. M.A. Lancaster, N.S. Corsini, S. Wolfinger, E.H. Gustafson, A.W. Phillips, T.R. Burkard, T. Otani, F.J. Livesey, J.A. Knoblich. Guided self-organization and cortical plate formation in human brain organoids, Nature Biotechnology. 35 (2017) 659–666. doi:10.1038/nbt.3906.

16. R. Simsa, T. Rothenbücher, H. Gürbüz, N. Ghosheh, J. Emneus, L. Jenndahl, D.L. Kaplan, N. Bergh, A.M. Serrano, P. Fogelstrand. Brain organoid formation on decellularized porcine brain ECM hydrogels, PLOS ONE. 16 (2021). doi:10.1371/journal.pone.0245685.

17. J. Bejoy, Z. Wang, B. Bijonowski, M. Yang, T. Ma, Q.-X. Sang, Y. Li. Differential effects of heparin and hyaluronic acid on neural patterning of human induced pluripotent stem cells, ACS Biomaterials Science & Engineering. 4 (2018) 4354–4366. doi:10.1021/acsbiomaterials.8b01142.

18. B.A. Lindborg, J.H. Brekke, A.L. Vegoe, C.B. Ulrich, K.T. Haider, S. Subramaniam, S.L. Venhuizen, C.R. Eide, P.J. Orchard, W. Chen, Q. Wang, F. Pelaez, C.M. Scott, E. Kokkoli, S.A. Keirstead, J.R. Dutton, J. Tolar, T.D. O'Brien. Rapid induction of cerebral organoids from human induced pluripotent stem cells using a chemically defined hydrogel and defined Cell Culture Medium, Stem Cells Translational Medicine. 5 (2016) 970–979. doi:10.5966/sctm.2015-0305.

19. J.D. Hartgerink, E. Beniash, S.I. Stupp, Peptide-amphiphile nanofibers: A versatile scaffold for the preparation of self-assembling materials, Proceedings of the National Academy of Sciences. 99 (2002) 5133–5138. doi:10.1073/pnas.072699999.

20. B. Derkus, B.O. Okesola, D.W. Barrett, M. D'Este, T.T. Chowdhury, D. Eglin, A. Mata. Multicomponent hydrogels for the formation of vascularized bone-like constructs in vitro, Acta Biomaterialia. 109 (2020) 82–94. doi:10.1016/j.actbio.2020.03.025.

21. S. Motamed, M.P. Del Borgo, K. Zhou, K. Kulkarni, P.J. Crack, T.D. Merson, M-I. Aguilar, D. I. Finkelstein, J.S. Forsythe. Migration and differentiation of neural stem cells diverted from the subventricular zone by an injectable self-assembling β-peptide hydrogel, Frontiers in Bioengineering and Biotechnology. 7 (2019). doi:10.3389/fbioe.2019.00315.

22. M. Isik, C.C. Eylem, T. Haciefendioglu, E. Yildirim, B. Sari, E. Nemutlu, E. Emregul, B. O. Okesola, B. Derkus. Mechanically robust hybrid hydrogels of photo-crosslinkable gelatin and laminin-mimetic peptide amphiphiles for neural induction, Biomaterials Science. 9 (2021) 8270–8284. doi:10.1039/d1bm01350e.

23. B.O. Okesola, S. Ni, B. Derkus, C.C. Galeano, A. Hasan, Y. Wu, J. Ramis, L. Buttery, J.I. Dawson, M. D'Este, R.O.C. Oreffo, D. Eglin, H. Sun, A. Mata, Growth-factor free multicomponent nanocomposite hydrogels that stimulate bone formation, Advanced Functional Materials. 30 (2020) 1906205. doi:10.1002/adfm.201906205.

24. A. Li, A. Hokugo, A. Yalom, E.J. Berns, N. Stephanopoulos, M.T. McClendon, L.A. Segovia, I. Spigelman, S.I. Stupp, R. Jarrahy. A bioengineered peripheral nerve construct using aligned peptide amphiphile nanofibers, Biomaterials. 35 (2014) 8780–8790. doi:10.1016/j.biomaterials.2014.06.049.

25. C.L. Hedegaard, C. Rodendo-Gomez, B.Y. Tan, K.W. Ng, D. Loessner, A. Mata. Peptide-protein coassembling matrices as a biomimetic 3D model of ovarian cancer, Science Advances 60, 40 (2020), eabb3298

26. D. Osuna De la Peña, S.M.D. Trabulo, E. Collin, Y. Liu, S. Sharma, M. Tatari, D. Behrens, M. Erkan, R.T. Lawlor, A. Scarpa, C. Heeschen, A. Mata, D. Loessner. Nature Communications 12 (2021) 5623.

27. D.E. Discher, D.J. Mooney, P.W. Zandstra, Growth factors, matrices, and forces combine and Control Stem Cells, Science. 324 (2009) 1673–1677. doi:10.1126/science.1171643.

28. S. Musah, P.J. Wrighton, Y. Zaltsman, X. Zhong, S. Zorn, M.B. Parlato, C. Hsiao, S.P. Palecek, Q. Chang, W.L. Murphy, L.L. Kiessling. Substratum-induced differentiation of human pluripotent stem cells reveals the coactivator yap is a potent regulator of neuronal specification, Proceedings of the National Academy of Sciences. 111 (2014) 13805–13810. doi:10.1073/pnas.1415330111.

29. A. Shkumatov, K. Baek, H. Kong, Matrix rigidity-modulated cardiovascular organoid formation from Embryoid Bodies, PLoS ONE. 9 (2014). doi:10.1371/journal.pone.0094764.

30. N. Gjorevski, N. Sachs, A. Manfrin, S. Giger, M.E. Bragina, P. Ordóñez-Morán, H. Clevers, M.P. Lutolf. Designer matrices for intestinal stem cell and organoid culture, Nature. 539 (2016) 560–564. doi:10.1038/nature20168.

31. G. Sorrentino, S. Rezakhani, E. Yildiz, S. Nuciforo, M.H. Heim, M.P. Lutolf, K. Schoonjans. Mechano-modulatory synthetic niches for liver organoid derivation, Nature Communications. 11 (2020). doi:10.1038/s41467-020-17161-0.

32. E. Prince, E. Kumacheva. Design and applications of man-made biomimetic fibrillary hydrogels. Nature Reviews Materials 4 (2019) 99–115.

33. A. J. Berger, K. L. Linsmeier, P. K. Kreeger, K. S. Masters. Decoupling the effects of stiffness and fiber density on cellular behaviors via an interpenetrating network of gelatin-methacrylate and collagen. Biomaterials 141 (2017) 125–135.

34. R. O. Hynes. The extracellular matrix: not just pretty fibrils. Science 326 (2009) 1216–1219.

35. C. Loebel, S.E. Szczesny, B.D. Cosgrove, M. Alini, M. Zenobi-Wong, R.L. Mauck, D. Eglin. Cross-linking chemistry of tyramine-modified hyaluronan hydrogels alters mesenchymal stem cell early attachment and behavior, Biomacromolecules. 18 (2017) 855–864. doi: 10.1021/acs.biomac.6b01740.

36. S. Kim, S. Min, Y.S. Choi, S-H. Jo, J. H. Jung, K. Han, J. Kim, S. An, Y. W. Ji, Y-G. Kim, S-W. Cho. Tissue extracellular matrix hydrogels as alternatives to Matrigel for culturing gastrointestinal organoids. Nature Communications. 13 (2022) 1692. doi.org/10.1038/s41467-022-29279-4

37. M. F. B. Jamaluddin, A. Ghosh, A. Ingle, R. Mohammed, A. Ali, M. Bahrami, G. Kaiko, Z. Gibb, E. C. Filipe, T. R. Cox, A. Boulton, R. O'Sullivan, Y. Lus, A. Karakoti, A. Vinu, P. Nahar, K. Jaaback, V. Bansal, P. S. Tanwar. Bovine and human endometrium-derived hydrogels support organoid culture from healthy and cancerous tissues. PNAS. 119 (2022) e2208040119. doi: org/10.1073/pnas.2208040119

38. C.C. Eylem, M. Yilmaz, B. Derkus, E. Nemutlu, C.B. Camci, E. Yilmaz, M.A. Turkoglu, B. Aytac, N. Ozyurt, E. Emregul. Untargeted multi-omic analysis of colorectal cancer-

specific exosomes reveals joint pathways of colorectal cancer in both clinical samples and cell culture, Cancer Letters. 469 (2020) 186–194. doi:10.1016/j.canlet.2019.10.038.

39. E.J. Berns, S. Sur, L. Pan, J.E. Goldberger, S. Suresh, S. Zhang, J.A. Kessler, S.I. Stupp. Aligned neurite outgrowth and directed cell migration in self-assembled monodomain gels, Biomaterials. 35 (2014) 185–195. doi:10.1016/j.biomaterials.2013.09.077.

40. R.M. Capito, H.S. Azevedo, Y.S. Velichko, A. Mata, S.I. Stupp, Self-assembly of large and small molecules into hierarchically ordered sacs and membranes, Science. 319 (2008) 1812–1816. doi:10.1126/science.1154586.

41. N.J. Greenfield, G.D. Fasman, Computed circular dichroism spectra for the evaluation of protein conformation, Biochemistry. 8 (1969) 4108–4116. doi:10.1021/bi00838a031.

42. S. Gerecht, J.A. Burdick, L.S. Ferreira, S.A. Townsend, R. Langer, G. Vunjak-Novakovic, Hyaluronic acid hydrogel for controlled self-renewal and differentiation of human embryonic stem cells, Proceedings of the National Academy of Sciences. 104 (2007) 11298–11303. doi:10.1073/pnas.0703723104.

43. S.L. Giandomenico, M. Sutcliffe, M.A. Lancaster, Generation and long-term culture of advanced cerebral organoids for studying later stages of neural development, Nature Protocols. 16 (2020) 579–602. doi:10.1038/s41596-020-00433-w.

44. Z. Zhang, P. Zhang, H. Hu, Large expression augments the glycosylation of glycoproteins in addition to α-dystroglycan conferring laminin binding, PLoS ONE. 6 (2011). doi:10.1371/journal.pone.0019080.

45. J. Hatakeyama, Y. Bessho, K. Katoh, S. Ookawara, M. Fujioka, F. Guillemot, R. Kageyema. *Hes* genes regulate size, shape and histogenesis of the nervous system by control of the timing of neural stem cell differentiation, Development. 131 (2004) 5539–5550. doi:10.1242/dev.01436.

46. Z. Sun, X. Xu, J. He, A. Murray, M.-an Sun, X. Wei, X. Wang, E. McCoig, E. Xie, X. Jiang, L. Li, J. Zhu, J. Chen, A. Morozov, A. M. Pickrell, M. H. Theus, H. Xie. EGR1 recruits TET1 to shape the brain methylome during development and upon neuronal activity, Nature Communications. 10 (2019). doi:10.1038/s41467-019-11905-3.

47. J. Baek, P.A. Lopez, S. Lee, T.-S. Kim, S. Kumar, D.V. Schaffer, *egr1* is a 3D matrix–specific mediator of mechanosensitive stem cell lineage commitment, Science Advances. 8 (2022). doi:10.1126/sciadv.abm4646.

48. E. Peco, T. Escude, E. Agius, V. Sabado, F. Medevielle, B. Ducommun, F. Pituello. The CDC25B phosphatase shortens the G2 phase of neural progenitors and promotes efficient neuron production, Development. 139 (2012) 1095–1104. doi:10.1242/dev.068569.

49. N. Kosi, I. Alić, M. Kolačević, N. Vrsaljko, N. Jovanov Milošević, M. Sobol, A. Philimonenko, P. Hozak, S. Gajovic, R. Pochet, D. Mitrecic. NOP2 is expressed during proliferation of neural stem cells and in adult mouse and human brain, Brain Research. 1597 (2015) 65–76. doi:10.1016/j.brainres.2014.11.040.

50. P. Romani, L. Valcarcel-Jimenez, C. Frezza, S. Dupont, Crosstalk between mechanotransduction and metabolism, Nature Reviews Molecular Cell Biology. 22 (2020) 22–38. doi:10.1038/s41580-020-00306-w.

51. R.P. Bazinet, S. Layé, Polyunsaturated fatty acids and their metabolites in brain function and disease, Nature Reviews Neuroscience. 15 (2014) 771–785. doi:10.1038/nrn3820.

52. M. Akbar, F. Calderon, Z. Wen, H.-Y. Kim, Docosahexaenoic acid: A positive modulator of Akt signaling in neuronal survival, Proceedings of the National Academy of Sciences. 102 (2005) 10858–10863. doi:10.1073/pnas.0502903102.

53. M. Guo, L. Stockert, M. Akbar, H.-Y. Kim, Neuronal specific increase of phosphatidylserine by docosahexaenoic acid, Journal of Molecular Neuroscience. 33 (2007) 67–73. doi:10.1007/s12031-007-0046-z.

54. R. Bertolio, F. Napoletano, M. Mano, S. Maurer-Stroh, M. Fantuz, A. Zannini, S. Bicciato, G. Sorrentino, G. Del Sal. Sterol regulatory element binding protein 1 couples mechanical cues and lipid metabolism, Nature Communications. 10 (2019). doi:10.1038/s41467-019-09152-7.

55. X. Jia, J. Song, W. Lv, J.P. Hill, J. Nakanishi, K. Ariga, Adaptive liquid interfaces induce neuronal differentiation of mesenchymal stem cells through lipid raft assembly, Nature Communications. 13 (2022). doi:10.1038/s41467-022-30622-y.

56. H. Ge, M. Tian, Q. Pei, F. Tan, H. Pei, Extracellular matrix stiffness: New areas affecting cell metabolism, Frontiers in Oncology. 11 (2021). doi:10.3389/fonc.2021.631991.

Figures

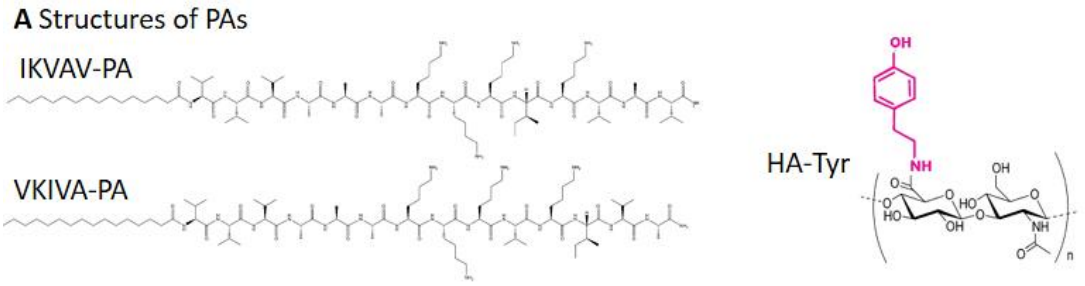

B Properties of components

PA	Sequence	Mw (Da)	Zeta potential (mV)
IKVAV-PA	$C_{15}H_{31}$-CONH-$V_3A_3K_3$IKVAV-$CONH_2$	1662	+12.3
VKIVA-PA	$C_{15}H_{31}$-CONH-$V_3A_3K_3$VKIVA-$CONH_2$	1662	+12.7
HA-Tyr		$2.9x10^5$	-31.1

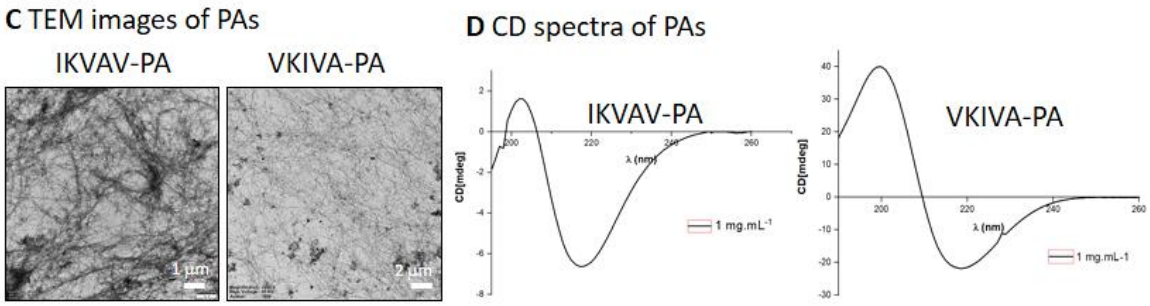

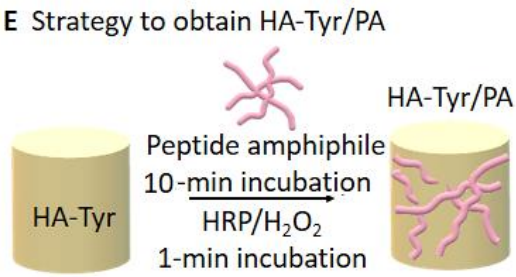

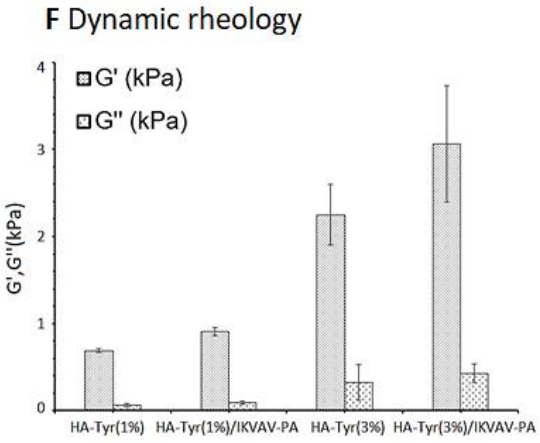

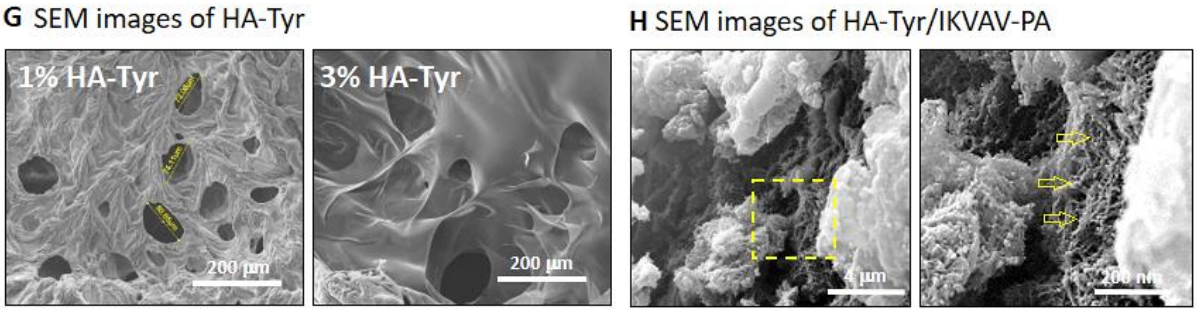

Figure 1

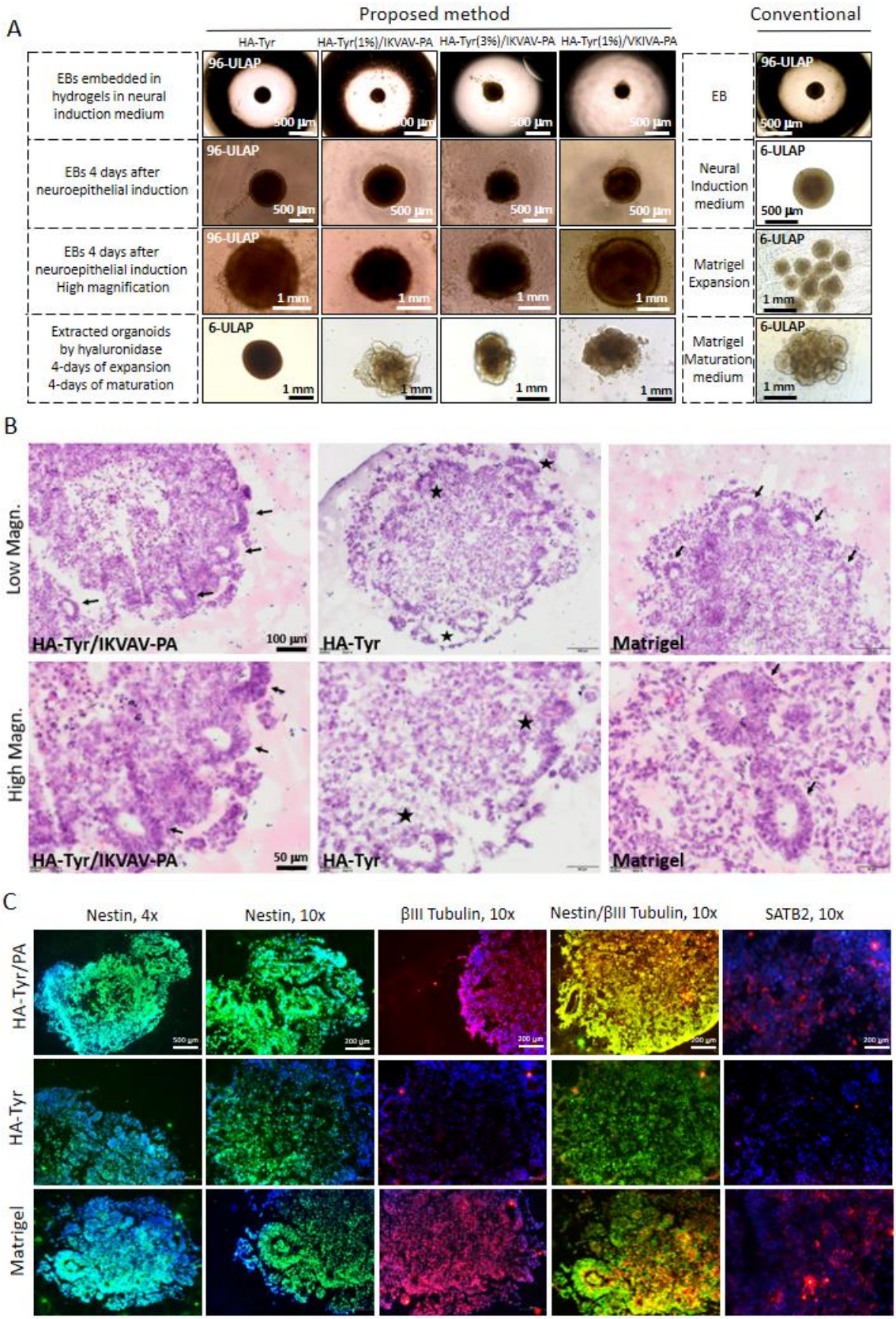
A
Proposed method
Conventional
HA-Tyr
HA-Tyr(1%)/IKVAV-PA
HA-Tyr(3%)/IKVAV-PA
HA-Tyr(1%)/VKIVA-PA
EBs embedded in hydrogels in neural induction medium
EBs 4 days after neuroepithelial induction
EBs 4 days after neuroepithelial induction High magnification
Extracted organoids by hyaluronidase 4-days of expansion 4-days of maturation
EB
Neural Induction medium
Matrigel Expansion
Matrigel Maturation medium
96-ULAP
6-ULAP
500 µm
1 mm
B
Low Magn.
High Magn.
HA-Tyr/IKVAV-PA
HA-Tyr
Matrigel
100 µm
50 µm
C
Nestin, 4x
Nestin, 10x
βIII Tubulin, 10x
Nestin/βIII Tubulin, 10x
SATB2, 10x
HA-Tyr/PA
HA-Tyr
Matrigel

Figure 2

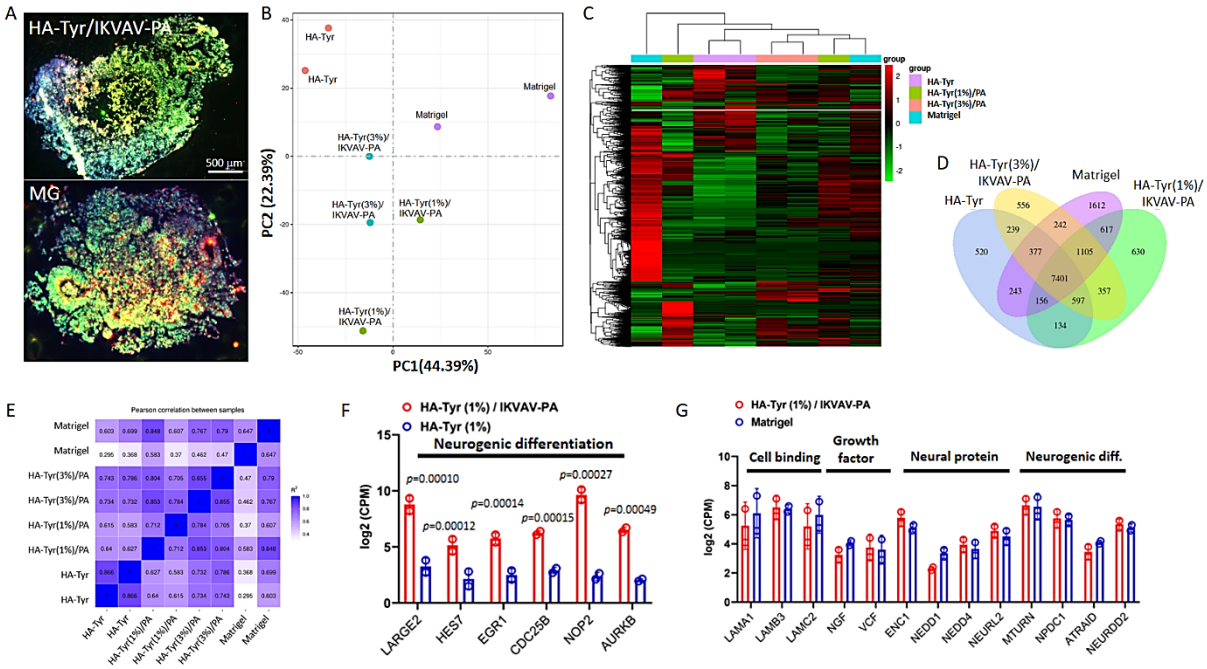
A
HA-Tyr/IKVAV-PA
500 μm
MG
B
HA-Tyr
HA-Tyr
Matrigel
Matrigel
HA-Tyr(3%)/ IKVAV-PA
HA-Tyr(3%)/ IKVAV-PA
HA-Tyr(1%)/ IKVAV-PA
HA-Tyr(1%)/ IKVAV-PA
PC2 (22.39%)
PC1(44.39%)
C
group
HA-Tyr
HA-Tyr(1%)/PA
HA-Tyr(3%)/PA
Matrigel
D
HA-Tyr(3%)/ IKVAV-PA
Matrigel
HA-Tyr(1%)/ IKVAV-PA
HA-Tyr
556
1612
239
242
617
520
377
1105
630
7401
243
156
597
357
134
E
Pearson correlation between samples
Matrigel
Matrigel
HA-Tyr(3%)/PA
HA-Tyr(3%)/PA
HA-Tyr(1%)/PA
HA-Tyr(1%)/PA
HA-Tyr
HA-Tyr
F
HA-Tyr (1%) / IKVAV-PA
HA-Tyr (1%)
Neurogenic differentiation
p=0.00010
p=0.00012
p=0.00014
p=0.00015
p=0.00027
p=0.00049
log2 (CPM)
LARGE2
HES7
EGR1
CDC25B
NOP2
AURKB
G
HA-Tyr (1%) / IKVAV-PA
Matrigel
Cell binding
Growth factor
Neural protein
Neurogenic diff.
log2 (CPM)
LAMA1
LAMB3
LAMC2
NGF
VCF
ENC1
NEDD1
NEDD4
NEURL2
MTURN
NPDC1
ATRAID
NEUROD2

Figure 3

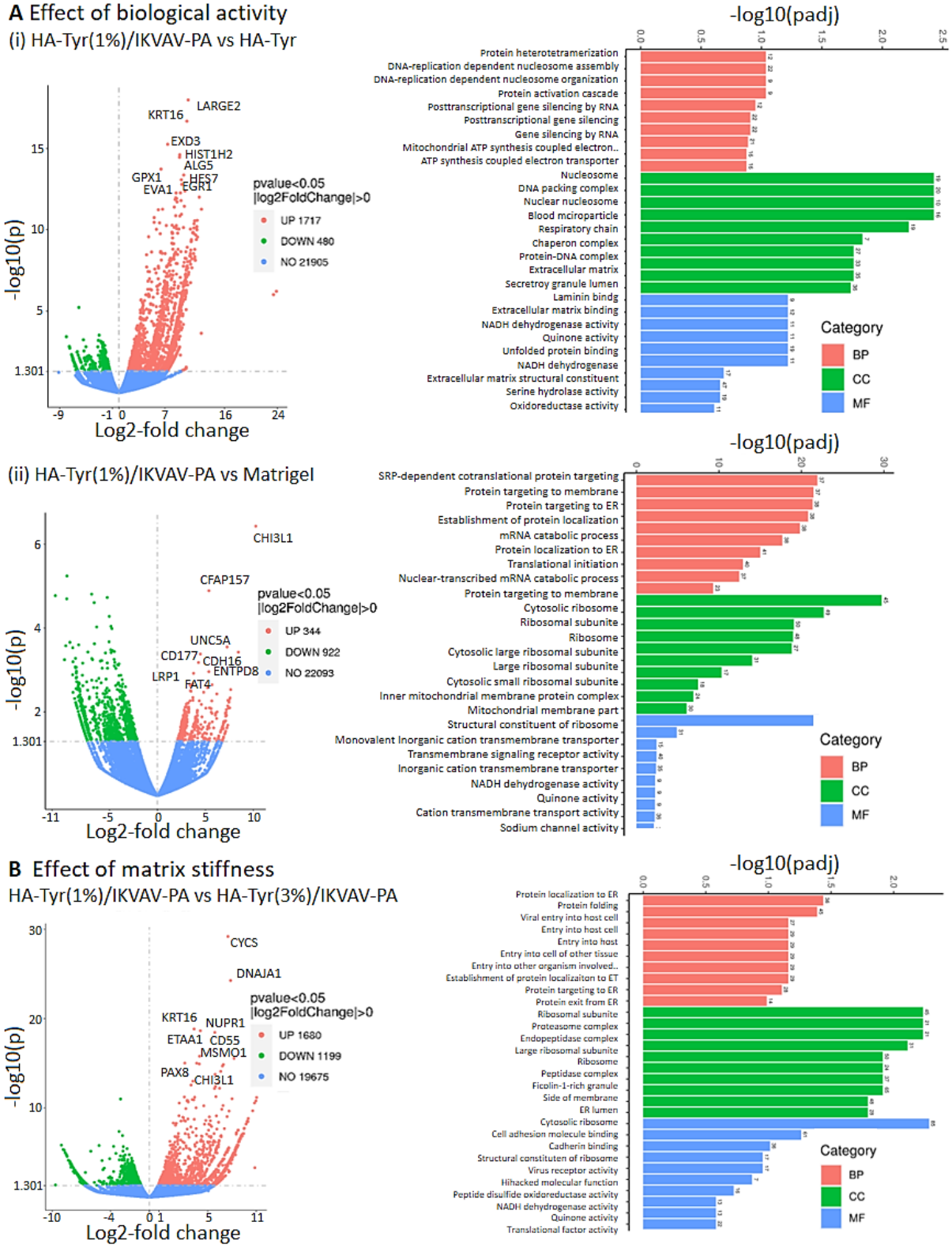
A Effect of biological activity
(i) HA-Tyr(1%)/IKVAV-PA vs HA-Tyr
-log10(p)
Log2-fold change
pvalue<0.05
|log2FoldChange|>0
UP 1717
DOWN 480
NO 21905
KRT16
LARGE2
EXD3
HIST1H2
ALG5
GPX1
HES7
EVA1
EGR1
-log10(padj)
Protein heterotetramerization
DNA-replication dependent nucleosome assembly
DNA-replication dependent nucleosome organization
Protein activation cascade
Posttranscriptional gene silencing by RNA
Posttranscriptional gene silencing
Gene silencing by RNA
Mitochondrial ATP synthesis coupled electron..
ATP synthesis coupled electron transporter
Nucleosome
DNA packing complex
Nuclear nucleosome
Blood mciroparticle
Respiratory chain
Chaperon complex
Protein-DNA complex
Extracellular matrix
Secretroy granule lumen
Laminin bindg
Extracellular matrix binding
NADH dehydrogenase activity
Quinone activity
Unfolded protein binding
NADH dehydrogenase
Extracellular matrix structural constituent
Serine hydrolase activity
Oxidoreductase activity
Category
BP
CC
MF
(ii) HA-Tyr(1%)/IKVAV-PA vs Matrigel
-log10(p)
Log2-fold change
pvalue<0.05
|log2FoldChange|>0
UP 344
DOWN 922
NO 22093
CHI3L1
CFAP157
UNC5A
CD177
CDH16
ENTPD8
LRP1
FAT4
-log10(padj)
SRP-dependent cotranslational protein targeting
Protein targeting to membrane
Protein targeting to ER
Establishment of protein localization
mRNA catabolic process
Protein localization to ER
Translational initiation
Nuclear-transcribed mRNA catabolic process
Protein targeting to membrane
Cytosolic ribosome
Ribosomal subunite
Ribosome
Cytosolic large ribosomal subunite
Large ribosomal subunite
Cytosolic small ribosomal subunite
Inner mitochondrial membrane protein complex
Mitochondrial membrane part
Structural constituent of ribosome
Monovalent Inorganic cation transmembrane transporter
Transmembrane signaling receptor activity
Inorganic cation transmembrane transporter
NADH dehydrogenase activity
Quinone activity
Cation transmembrane transport activity
Sodium channel activity
Category
BP
CC
MF
B Effect of matrix stiffness
HA-Tyr(1%)/IKVAV-PA vs HA-Tyr(3%)/IKVAV-PA
-log10(p)
Log2-fold change
pvalue<0.05
|log2FoldChange|>0
UP 1680
DOWN 1199
NO 19675
CYCS
DNAJA1
KRT16
NUPR1
ETAA1
CD55
MSMO1
PAX8
CHI3L1
-log10(padj)
Protein localization to ER
Protein folding
Viral entry into host cell
Entry into host cell
Entry into host
Entry into cell of other tissue
Entry into other organism involved..
Establishment of protein localizaiton to ET
Protein targeting to ER
Protein exit from ER
Ribosomal subunite
Proteasome complex
Endopeptidase complex
Large ribosomal subunite
Ribosome
Peptidase complex
Ficolin-1-rich granule
Side of membrane
ER lumen
Cytosolic ribosome
Cell adhesion molecule binding
Cadherin binding
Structural constituten of ribosome
Virus receptor activity
Hihacked molecular function
Peptide disulfide oxidoreductase activity
NADH dehydrogenase activity
Quinone activity
Translational factor activity
Category
BP
CC
MF

Figure 4

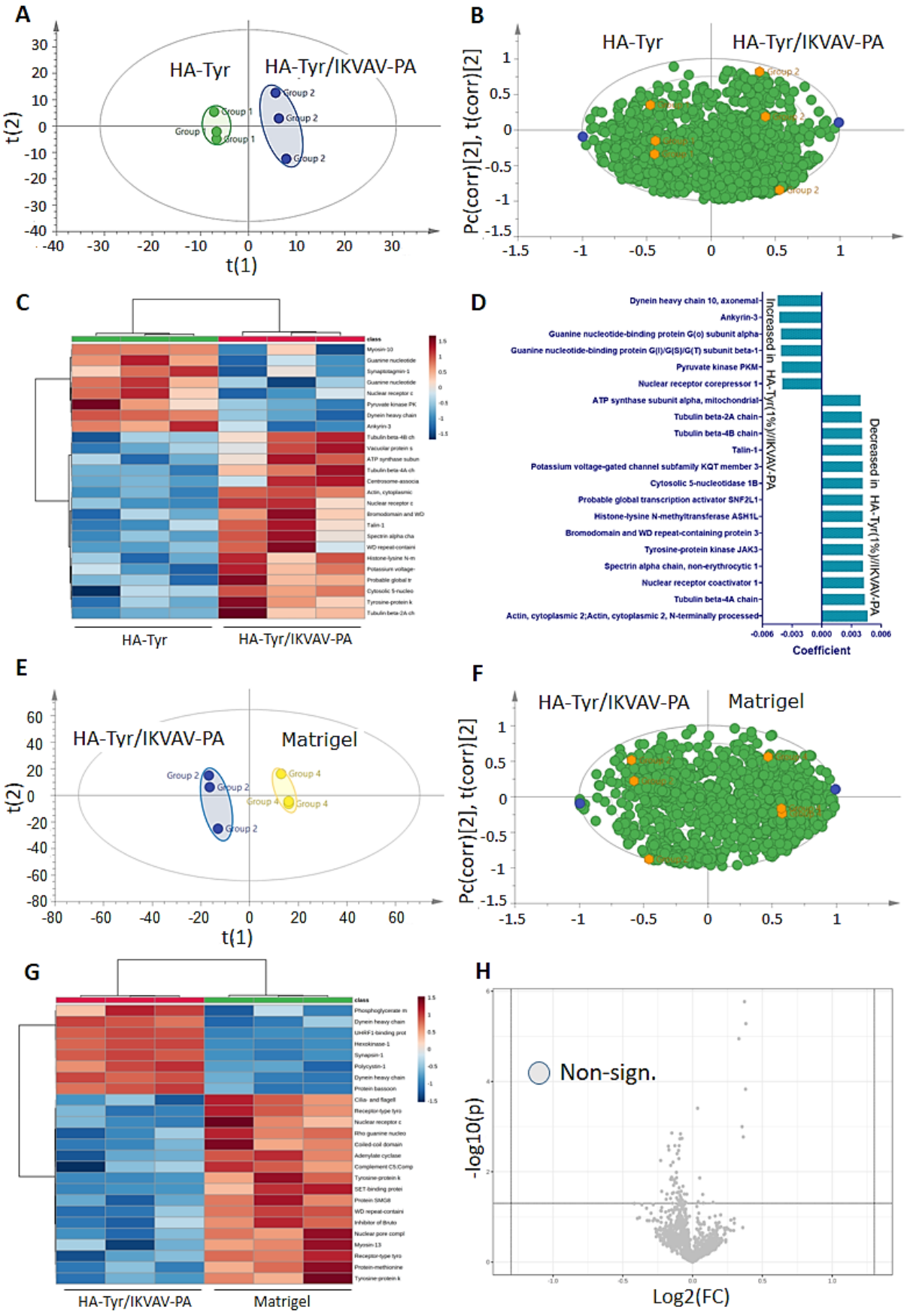
A
HA-Tyr
HA-Tyr/IKVAV-PA
t(2)
t(1)
B
HA-Tyr
HA-Tyr/IKVAV-PA
Pc(corr)[2], t(corr)[2]
C
HA-Tyr
HA-Tyr/IKVAV-PA
D
Dynein heavy chain 10, axonemal
Ankyrin-3
Guanine nucleotide-binding protein G(o) subunit alpha
Guanine nucleotide-binding protein G(I)/G(S)/G(T) subunit beta-1
Pyruvate kinase PKM
Nuclear receptor corepressor 1
ATP synthase subunit alpha, mitochondrial
Tubulin beta-2A chain
Tubulin beta-4B chain
Talin-1
Potassium voltage-gated channel subfamily KQT member 3
Cytosolic 5-nucleotidase 1B
Probable global transcription activator SNF2L1
Histone-lysine N-methyltransferase ASH1L
Bromodomain and WD repeat-containing protein 3
Tyrosine-protein kinase JAK3
Spectrin alpha chain, non-erythrocytic 1
Nuclear receptor coactivator 1
Tubulin beta-4A chain
Actin, cytoplasmic 2;Actin, cytoplasmic 2, N-terminally processed
Increased in HA-Tyr(1%)/IKVAV-PA
Decreased in HA-Tyr(1%)/IKVAV-PA
Coefficient
E
HA-Tyr/IKVAV-PA
Matrigel
t(2)
t(1)
F
HA-Tyr/IKVAV-PA
Matrigel
Pc(corr)[2], t(corr)[2]
G
HA-Tyr/IKVAV-PA
Matrigel
H
Non-sign.
-log10(p)
Log2(FC)

Figure 5

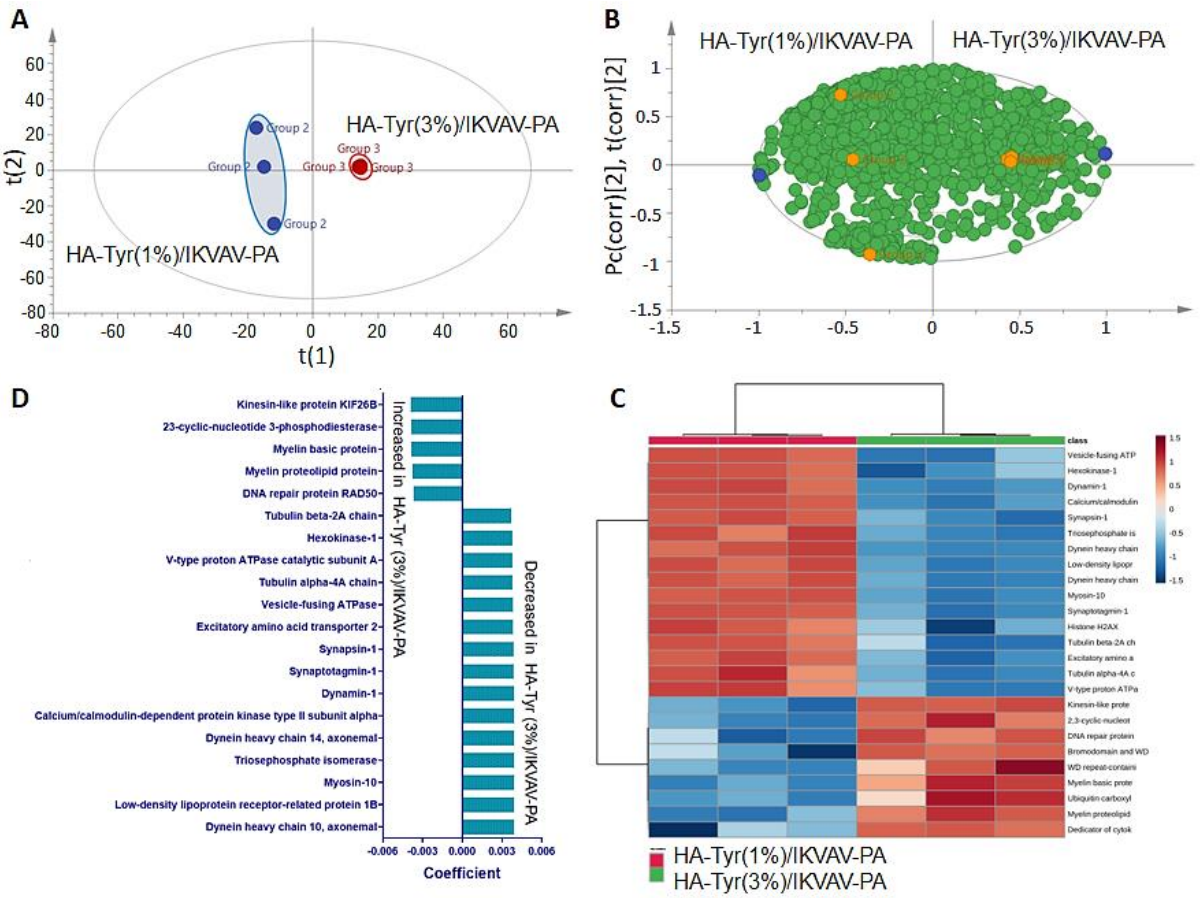
A
HA-Tyr(3%)/IKVAV-PA
HA-Tyr(1%)/IKVAV-PA
t(1)
t(2)
B
HA-Tyr(1%)/IKVAV-PA
HA-Tyr(3%)/IKVAV-PA
Pc(corr)[2], t(corr)[2]
C
HA-Tyr(1%)/IKVAV-PA
HA-Tyr(3%)/IKVAV-PA
D
Kinesin-like protein KIF26B
23-cyclic-nucleotide 3-phosphodiesterase
Myelin basic protein
Myelin proteolipid protein
DNA repair protein RAD50
Tubulin beta-2A chain
Hexokinase-1
V-type proton ATPase catalytic subunit A
Tubulin alpha-4A chain
Vesicle-fusing ATPase
Excitatory amino acid transporter 2
Synapsin-1
Synaptotagmin-1
Dynamin-1
Calcium/calmodulin-dependent protein kinase type II subunit alpha
Dynein heavy chain 14, axonemal
Triosephosphate isomerase
Myosin-10
Low-density lipoprotein receptor-related protein 1B
Dynein heavy chain 10, axonemal
Increased in HA-Tyr (3%)/IKVAV-PA
Decreased in HA-Tyr (3%)/IKVAV-PA
Coefficient

Figure 6

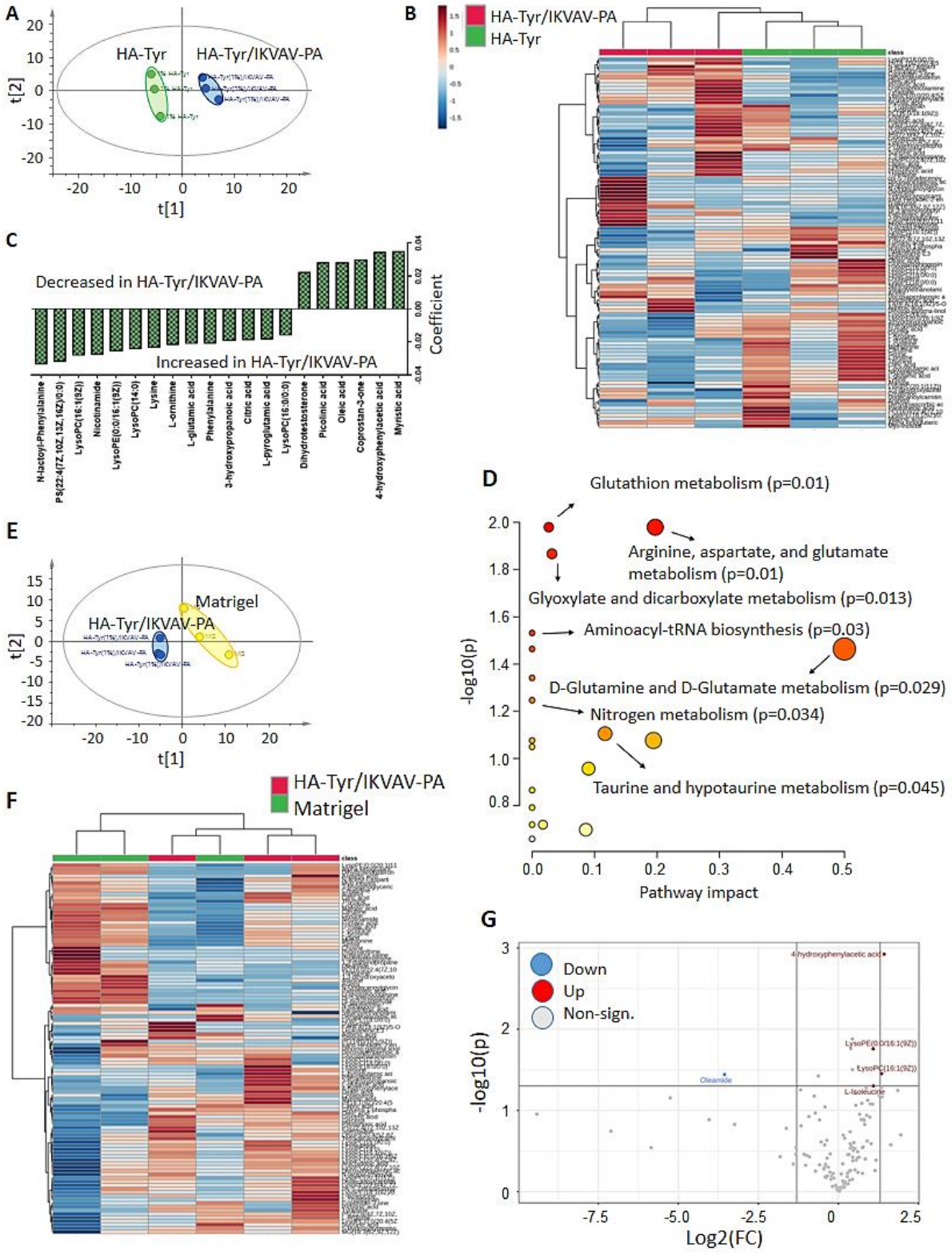
A
HA-Tyr
HA-Tyr/IKVAV-PA
t[1]
t[2]
B
HA-Tyr/IKVAV-PA
HA-Tyr
C
Decreased in HA-Tyr/IKVAV-PA
Increased in HA-Tyr/IKVAV-PA
Coefficient
N-lactoyl-Phenylalanine
PS(22:4(7Z,10Z,13Z,16Z)/0:0)
LysoPC(16:1(9Z))
Nicotinamide
LysoPE(0:0/16:1(9Z))
LysoPC(14:0)
Lysine
L-ornithine
L-glutamic acid
Phenylalanine
3-hydroxypropanoic acid
Citric acid
L-pyroglutamic acid
LysoPC(16:0/0:0)
Dihydrotestosterone
Picolinic acid
Oleic acid
Coprostan-3-one
4-hydroxyphenylacetic acid
Myristic acid
D
Glutathion metabolism (p=0.01)
Arginine, aspartate, and glutamate metabolism (p=0.01)
Glyoxylate and dicarboxylate metabolism (p=0.013)
Aminoacyl-tRNA biosynthesis (p=0.03)
D-Glutamine and D-Glutamate metabolism (p=0.029)
Nitrogen metabolism (p=0.034)
Taurine and hypotaurine metabolism (p=0.045)
-log10(p)
Pathway impact
E
Matrigel
HA-Tyr/IKVAV-PA
t[1]
t[2]
F
HA-Tyr/IKVAV-PA
Matrigel
G
Down
Up
Non-sign.
4-hydroxyphenylacetic acid
LysoPE(0:0/16:1(9Z))
LysoPC(16:1(9Z))
Oleamide
L-Isoleucine
-log10(p)
Log2(FC)

Figure 7

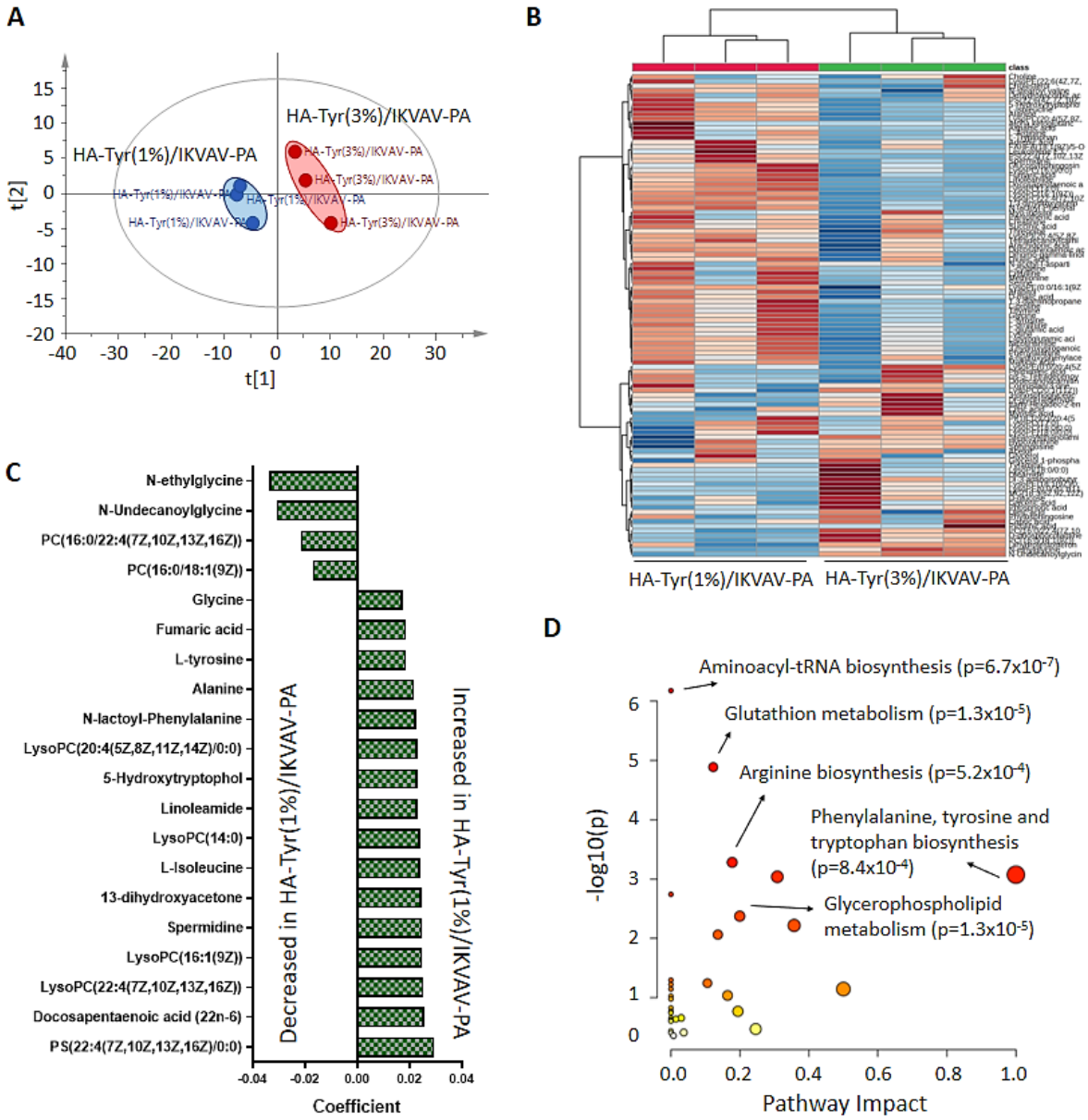
A
HA-Tyr(3%)/IKVAV-PA
HA-Tyr(1%)/IKVAV-PA
t[1]
t[2]
B
HA-Tyr(1%)/IKVAV-PA
HA-Tyr(3%)/IKVAV-PA
C
N-ethylglycine
N-Undecanoylglycine
PC(16:0/22:4(7Z,10Z,13Z,16Z))
PC(16:0/18:1(9Z))
Glycine
Fumaric acid
L-tyrosine
Alanine
N-lactoyl-Phenylalanine
LysoPC(20:4(5Z,8Z,11Z,14Z)/0:0)
5-Hydroxytryptophol
Linoleamide
LysoPC(14:0)
L-Isoleucine
13-dihydroxyacetone
Spermidine
LysoPC(16:1(9Z))
LysoPC(22:4(7Z,10Z,13Z,16Z))
Docosapentaenoic acid (22n-6)
PS(22:4(7Z,10Z,13Z,16Z)/0:0)
Decreased in HA-Tyr(1%)/IKVAV-PA
Increased in HA-Tyr(1%)/IKVAV-PA
Coefficient
D
Aminoacyl-tRNA biosynthesis (p=6.7x10-7)
Glutathion metabolism (p=1.3x10-5)
Arginine biosynthesis (p=5.2x10-4)
Phenylalanine, tyrosine and tryptophan biosynthesis (p=8.4x10-4)
Glycerophospholipid metabolism (p=1.3x10-5)
-log10(p)
Pathway Impact

Figure 8